Final submitted version
Soft Robotics, 17 Dec 2020
DOI 10.1089/soro.2019.0053

Lightweight, Highly-Tunable Jamming-Based Composites

Yashraj S. Narang[1,2], Buse Aktaş[1], Sarah Ornellas[3], Joost J. Vlassak[1], and Robert D. Howe[1*]

[1]Paulson School of Engineering and Applied Sciences, Harvard University, Cambridge, MA 02138
[2]NVIDIA Corporation, Seattle, WA 98105
[3]School of Engineering & Applied Science, Yale University, New Haven, CT 06511
[*]Corresponding author: Email howe@seas.harvard.edu

Abstract

Tunable-impedance mechanisms can improve the adaptivity, robustness, and efficiency of a vast array of engineering systems and soft robots. In this paper, we introduce a tunable-stiffness mechanism called a "sandwich jamming structure," which fuses the exceptional stiffness range of state-of-the-art laminar jamming structures (also known as layer jamming structures) with the high stiffness-to-mass ratios of classical sandwich composites. We experimentally develop sandwich jamming structures with performance-to-mass ratios that are far greater than laminar jamming structures (e.g., a 550-fold increase in stiffness-to-mass ratio), while simultaneously achieving tunable behavior that standard sandwich composites inherently cannot achieve (e.g., a rapid and reversible 1800-fold increase in stiffness). Through theoretical and computational models, we then show that these ratios can be augmented by several orders of magnitude further, and we provide an optimization routine that allows designers to build the best-possible sandwich jamming structures given arbitrary mass, volume, and material constraints. Finally, we demonstrate the utility of sandwich jamming structures by integrating them into a wearable soft robot (i.e., a tunable-stiffness wrist orthosis) that has negligible impact on the user in the off-state, but can reduce muscle activation by an average of 65% in the on-state. Through these theoretical and experimental investigations, we show that sandwich jamming structures are a lightweight, highly-tunable mechanism that can markedly extend the performance limits of existing structures and devices.

1 Introduction

TUNABLE-IMPEDANCE mechanisms (e.g., tunable-stiffness materials and struc-

tures) can improve the adaptivity, safety, robustness, and energy efficiency of a diverse array of engineering systems[1]. One class of tunable-impedance mechanisms is jamming structures. In comparison to other such mechanisms, these structures have high impedance range, impedance resolution, conformability in the unactivated state, and activation speed, as well as low cost and difficulty of fabrication [2, 3, 4]. Jamming structures have been effectively used in robotic manipulators[5, 6, 7, 4], haptic interfaces[8, 9, 10, 11, 12], medical devices[13, 2, 14, 15], and locomotion and aerospace structures[16, 17, 18].

Research on jamming mechanisms has primarily focused on two types of structures: granular jamming structures and laminar jamming (a.k.a., "layer jamming") structures. Granular jamming structures typically consist of collections of particles (e.g., coffee grounds) enclosed in an airtight envelope. When vacuum is applied to the envelope, kinematic and frictional coupling increase, augmenting the stiffness and damping of the structure. The jammed structures are highly resistant to compression and shear loads, but inherently fragile in tension and bending due to particle separation and dislocations[14, 15, 19].

Similarly, laminar jamming structures typically consist of flexible layers, usually of a single type of material (e.g., strips of fabric), enclosed in an airtight envelope. When vacuum is applied, frictional coupling increases, again augmenting the stiffness and damping of the structure. Laminar jamming structures are exceptionally resistant to bending[4]; furthermore, they have an inherently thin, lightweight form factor. These properties make laminar jamming structures particularly suitable for integration into tunable soft robotic manipulators and wearable devices, which often require high maximum bending stiffness and low physical profile, both relative to mass.

There are numerous applications in which mass is critical; these applications demand laminar jamming structures with even higher performance-to-mass ratios. For example, in assistive devices, researchers have used laminar jamming structures to selectively immobilize injured joints[20, 21]. However, as documented in previous work[8, 4], laminar jamming structures begin to yield (i.e., exhibit a decreased bending stiffness) after a critical transverse load is exceeded and adjacent layers start to slide. To prevent yielding, the structures can be thickened, but it is well established that adding mass to the body increases metabolic energy expenditure[22, 23]. As a second example, in quadcopter design, laminar jamming structures have been used to construct landing gear with a tunable impact response[18]. However, the lift-to-drag ratio of aerial vehicles decreases monotonically and dramatically with higher mass[24]. As these cases demonstrate, minimizing the mass of laminar jamming structures is often essential for practical use.

To improve the performance-to-mass of laminar jamming structures, we introduce the concept of *sandwich jamming structures*. Sandwich jamming structures are inspired by standard sandwich panels, which comprise one of the fundamental categories of modern composites. Sandwich panels consist of thin, stiff faces (made of materials such as aluminum) permanently bonded to a thick, low-density core (made of materials such as polyethylene). Due to the geometric separation of the stiff faces (analogous to an I-

beam) and the shear and buckling resistance of the core, the combination has outstanding stiffness-to-mass properties. These structures first came into widespread use during the initial development of military aircraft, and they have since been applied to industries as diverse as construction, automobile engineering, and spacecraft design[25].

The *sandwich jamming structures* presented here take the form of sandwich panels, as they consist of stiff face material and compliant core material. However, like laminar jamming structures, the faces and core are divided into numerous unbonded laminae, all enclosed within an airtight envelope (**Figure 1A**). When no vacuum is applied, the structure is highly compliant; however, when vacuum is applied, frictional coupling dramatically increases between the laminae, and the structure effectively transforms into a sandwich panel. As we show, sandwich jamming structures have far higher performance-to-mass ratios than laminar jamming structures—specifically, higher maximum stiffness, stiffness range (i.e., the ratio of the jammed to unjammed stiffness), and yield force, all with respect to mass. Such performance also greatly exceeds that of other tunable sandwich structures in the literature[26, 27, 28, 29, 30].

Furthermore, sandwich jamming structures are far more mechanically versatile than standard sandwich panels. They can adapt their stiffness and damping to the environment (e.g., as aerodynamic and hydrodynamic control surfaces), can be molded to an arbitrary initial shape (e.g., when conforming to the body), and can recover their undeformed configuration after yielding (e.g., after impacts). In summary, sandwich jamming structures have far higher performance-to-mass ratios than laminar jamming structures, as well as far greater versatility than sandwich panels.

2 Objective

In this paper, we first experimentally demonstrate that sandwich jamming structures have far higher performance-to-mass ratios than laminar jamming analogues. We then present detailed theoretical and finite-element models that parametrically describe how and to what extent laminar jamming structures can be improved by converting them to a sandwich jamming architecture. Next, we provide an optimization tool that allows designers to input an arbitrary set of materials and mass-volume constraints and then identify the highest-performance sandwich jamming structure that can be constructed within those bounds. Finally, we demonstrate the utility of sandwich jamming structures by integrating them into a wearable soft robot (i.e., a lightweight, conformable, tunable-stiffness wrist orthosis) that can markedly reduce muscle activation when turned on and preserve natural range of motion when turned off.

Through this work, we contribute the concept of tunable jamming-based sandwich structures, which in general, also comprise one of the first examples of jamming-based composites. Furthermore, we impart designers with an analysis and simulation toolkit that allows them to relate the design parameters of sandwich jamming structures (e.g., the number of layers in the face and core) to performance specifications (e.g, stiffness range), as well as optimize the performance of the structures. Overall, we demonstrate

that sandwich jamming structures can advance the state-of-the-art in tunable-stiffness mechanisms, and we provide the means to further their development within soft robotics and other fields.

3 Materials and Methods

The following is a highly abridged description of the materials and methods used in this study. For complete detail, please see **Supporting Information**.

3.1 Experimental Proof-of-Concept

To validate the concept of sandwich jamming structures, prototypes were constructed and experimentally characterized. The primary goal of the investigation was to determine whether sandwich jamming structures could achieve higher performance-to-mass ratios than laminar jamming structures. As described earlier, each sandwich structure consisted of faces composed of unbonded stiff laminae and a core composed of unbonded, compliant, lightweight laminae, all within an airtight envelope. When no vacuum is applied, the structure is highly compliant, and when vacuum is applied, the structure effectively transforms into a standard sandwich panel. Accordingly, the heuristics of modern sandwich panel construction were followed[31, 25]. Specifically, all sandwich jamming structures were constructed such that the small-deformation stress-strain modulus of the face material was at least an order of magnitude greater than that of the core material, and the total thickness of the core was at least an order of magnitude greater than the total thickness of the faces.

Paper, polyurethane (PU) foam, low-density polyethylene (LDPE), and low-carbon steel were chosen as candidate materials for the face and core, as the materials were low cost, exhibited negligible electrostatic attraction, and could be effectively cut using standard laboratory equipment. Specifically, sandwich jamming structures were fabricated with the following material configurations: 1) low-carbon steel face laminae and paper core laminae (**Figure 1B-C**), 2) low-carbon steel face laminae and low-density polyethylene (LDPE) core laminae, and 3) paper face laminae and polyurethane (PU) foam core laminae. For each material configuration, structures were built using various numbers of core layers.

Multiple samples were fabricated for each material configuration. For each sample, individual laminae were cut from raw stock using a laser cutter (VLS4.60, Universal Laser Systems, Inc., Scottsdale, AZ), metal shears, or razor blades. The laminae were stacked and placed inside an airtight thermoplastic elastomer (TPE) envelope (Fibre Glast Developments Corp., Brookville, OH). The envelope was sealed using an impulse sealer (AIE-450FD, American International Electric Inc., City of Industry, CA), and a plastic tube was inserted as a vacuum line.

Each sample was placed onto a universal materials testing device (Instron 5566, Illinois Tool Works, Norwood, MA), and the desired vacuum pressure was applied or removed using a manual vacuum regulator in order to activate or deactivate jamming, respectively. The sample was then loaded in 3-point bending (**Figure 2A**), and the force-versus-deflection relationships were measured during loading and unloading.

Three performance metrics were extracted from the experimental data: jammed stiffness, stiffness range (i.e., the ratio of jammed to unjammed stiffnesses), and yield force (i.e., the transverse force at which the jammed stiffness tends to decrease due to sliding between the layers), all divided by mass. Using previously-reported theory[4], the same performance metrics were calculated for laminar jamming structures consisting of just the face laminae. The performance metrics of the sandwich jamming structures were then divided by the corresponding values for the laminar jamming structures. (For example, the performance metrics for a sandwich jamming structure consisting of 2 layers of steel, 20 layers of paper, and 2 layers of steel were divided by the corresponding values for a laminar jamming structure consisting of 4 layers of steel.) These quotients comprised "improvement ratios" that described how much higher the performance metrics of the sandwich jamming structures were in comparison to corresponding laminar jamming structures.

3.2 Theoretical Modeling

Following the experimental proof-of-concept, a general question was considered: given a set of laminar jamming structures (e.g., ones that have been selected for a specific application), by what factor can their performance metrics be improved by converting them to sandwich jamming structures? In equivalent terms, what are the best-case experimental "improvement ratios"? To answer this question, theoretical expressions for the improvement ratios were derived. The expressions were intended to articulate exactly how these ratios scale with critical design parameters (e.g., elastic moduli of the faces), providing the basis for subsequent design optimization.

The most basic strategy to convert a laminar jamming structure into a sandwich jamming structure is to simply add core layers. However, in the real world, this strategy may be infeasible due to strict mass and volume constraints. For generality, all modeling was repeated for three different constraints that are relevant when converting laminar jamming structures into sandwich jamming structures. These constraints are as follows:

1. An "equal-material" constraint, in which maintaining cost is the primary concern. *All* the sheets of the laminar jamming structure are used as face laminae for the sandwich jamming structure, and core laminae (which are relatively compliant and typically far less expensive) can be added arbitrarily (**Figure 3A**). Note that this strategy is the "most basic strategy" just mentioned.

2. An "equal-mass" constraint, in which preserving mass is the primary concern. A *subset* of the sheets of the laminar jamming structure are used as face laminae for the sandwich jamming structure, and core laminae can be added with the constraint that the total *mass* of the sandwich must be equal to the mass of the laminar jamming structure (**SI: Figure S2A**).

3. An "equal-volume" constraint, in which preserving volume is the primary concern. A *subset* of the sheets of the laminar jamming structure are used as face laminae for the sandwich jamming structure, and core laminae can be added with

the constraint that the total *volume* of the sandwich must be equal to the volume of the laminar jamming structure (**SI: Figure S3A**).

For sake of brevity, this section only provides formulae for improvement ratios given an "equal-material" constraint; a detailed consideration of the equal-mass and equal-volume constraints is included in **SI: Theoretical Modeling**.

In order to determine how the performance-to-mass metrics of standard laminar jamming structures could be improved by converting them to a sandwich architecture (with an equal-material constraint), the theoretical performance-to-mass of both types of structures was first calculated. As in the experimental proof-of-concept, three performance-to-mass metrics were computed: 1) maximum bending stiffness, 2) bending stiffness range, and 3) yield force, all divided by mass. Ratios were then computed of the performance-to-mass metrics of the sandwich jamming structure to the corresponding metrics of a standard laminar jamming structure. The ratios were expressed as functions of critical non-dimensional design parameters.

For standard laminar jamming structures, the performance metrics were calculated using classical (i.e., Euler-Bernoulli) beam theory. An excellent discussion of classical beam theory is provided in [32], and a detailed description of how to apply the theory to laminar jamming structures is provided in [4]. For sandwich jamming structures, the performance metrics were calculated using sandwich beam theory, a well-established theory in structural mechanics used for predicting the load-deformation relationships of sandwich panels. Sandwich theory is based on Timoshenko beam theory, which itself extends classical theory to include the effects of shear deformations within beams. However, sandwich theory makes the additional assumptions that 1) the beam consists of 2 faces and a core, 2) the faces are much thinner than the core, and 3) the core is much more compliant than the faces. Excellent references on sandwich theory include [33, 34, 31, 25], and the following paragraphs summarize key formulae that result from applying sandwich theory to sandwich jamming structures. Please note that step-by-step derivations are provided in **SI: Theoretical Modeling**.

From sandwich theory, the jammed stiffness of a sandwich jamming structure (i.e., a solid sandwich beam) is approximately $E_f b\frac{4c^2f+4cf^2+f^3}{16}$, where E_f is the elastic modulus of the face material; b is the width; and c and f are the total thickness of the core and face, respectively. From classical beam theory, the jammed stiffness of a laminar jamming structure (i.e., a solid standard beam) is $\frac{EbH^3}{12}$, where E is the elastic modulus of the layers and H is the total thickness. We used these expressions to algebraically derive the stiffness-to-mass improvement ratio, which is

$$\left(\frac{k_b}{m}\right)^* = \frac{12(\frac{c}{f})^2 + 12\frac{c}{f} + 3}{4(\frac{\rho_c}{\rho_f}\frac{c}{f} + 1)} \qquad (1)$$

where $(\frac{k_b}{m})^*$ is the dimensionless ratio of the bending-stiffness-to-mass of the sandwich jamming structure to that of the laminar jamming structure, $\frac{c}{f}$ is the ratio of the total thickness of the core to that of the faces; and $\frac{\rho_c}{\rho_f}$ is the ratio of the density of the core material to the density of the face material.

To calculate the range of a jamming structure, the unjammed stiffness must be computed as well. From classical beam theory, the unjammed stiffness of a sandwich jamming structure (i.e., a decoupled stack of solid sandwich beams) is $b\frac{E_c n_c h_c^3 + E_f n_f h_f^3}{12}$, where E_c is the elastic modulus of the core; n_c and n_f are the total number of layers in the core and faces, respectively; and h_c and h_f are the thickness of each core and face layer, respectively. The unjammed stiffness of a laminar jamming structure (i.e., a decoupled stack of solid standard beams) is $\frac{Ebnh^3}{12}$. We used these expressions to algebraically derive the range-to-mass improvement ratio, which is

$$\left(\frac{r}{m}\right)^* = \frac{12(\frac{c}{f})^2 + 12\frac{c}{f} + 3}{4(\frac{E_c}{E_f}(\frac{h_c}{h_f})^2\frac{c}{f} + 1)(\frac{\rho_c}{\rho_f}\frac{c}{f} + 1)} \quad (2)$$

where $(\frac{r}{m})^*$ is the ratio of the range-to-mass of the sandwich jamming structure to that of the laminar jamming structure, and $\frac{E_c}{E_f}$ is the ratio of the elastic modulus of the core material to that of the face material.

Finally, to calculate the yield force of a jamming structure, the maximum induced shear stress must be equated with the maximum allowable shear stress (as limited by friction and pressure). For a sandwich jamming structure, we derived the yield force to be approximately $2bc\mu_c P$, where μ_c is the coefficient of friction of the core material and P is the vacuum pressure; for a laminar jamming structure, the yield force is $\frac{4}{3}bH\mu P$, where μ is the coefficient of friction of the layers[4]. We used these expressions to derive the yield-to-mass improvement ratio, which is

$$\left(\frac{F_{crit}}{m}\right)^* = \frac{3}{2}\frac{\mu_c}{\mu_f}\frac{\frac{c}{f}}{\frac{\rho_c}{\rho_f}\frac{c}{f} + 1} \quad (3)$$

where $(\frac{F_{crit}}{m})^*$ is the ratio of the yield force of the sandwich jamming structure to that of the laminar jamming structure, and $\frac{\mu_c}{\mu_f}$ is the ratio of the coefficient of friction of the core material to that of the face material.

3.3 Validation of Theoretical Model

Finite element simulations were conducted to corroborate the predictions of the theoretical model. Simulations were generated and executed using commercial simulation software (Abaqus 2017, Dassault Systèmes, Vélizy-Villacoublay, France). Each layer was modeled as a 2-dimensional body, and frictional contact was prescribed at the interfaces between adjacent layers. A uniform mesh of quadrilateral elements was used, with 2 elements across the thickness of each face layer. Vacuum pressure was applied, and the structures were loaded in 3-point bending (**Figure 4A-C**). A static implicit solver was selected, and large-deformation analysis and automatic time-stepping were enabled.

The simulations were executed over a range of design parameters that could be achieved with common laboratory materials (e.g., standard metals and plastics). Since the simulations were static rather than dynamic, inertia was negligible; thus, the density ratio was not varied, as it did not affect the output. All parameters used in the simulations are tabulated in **SI: Validation of Theoretical Model: Finite Element Analysis**.

From the simulations, force-versus-deflection curves were extracted. As with the experimental data, the stiffness, range, and yield forces were extracted from these curves.

Experimental tests were also conducted to evaluate the predictions of the theoretical

model for a steel-paper sandwich jamming structure. The experimental procedure was nearly identical to that described earlier for testing of initial prototypes in **Materials and Methods: Experimental Proof-of-Concept**. Further details are provided in **SI: Validation of Theoretical Model: Experimental Comparison**.

3.4 Optimization

The preceding analysis and simulations determined exactly how and to what extent given laminar jamming structures can be improved by converting them to a sandwich architecture (i.e., by adding a core). However, for a designer who is building sandwich jamming structures from the ground-up, it is also important to identify the sandwich jamming structure with the best-possible performance-to-mass ratios, rather than the best-possible improvement ratio over a given laminar jamming structure. Furthermore, the designer may be constrained by a maximum mass, a maximum volume, and a particular set of real-world materials.

This problem is theoretically challenging for two major reasons. First, although performance improvement ratios (e.g., stiffness-to-mass improvement ratio) are dimensionless and can be expressed as a function of a small number of non-dimensional parameters (e.g, $\frac{\rho_c}{\rho_f}$), performance metrics themselves (e.g., stiffness-to-mass ratio) are dimensional and cannot be analogously simplified (e.g., the absolute magnitudes of both ρ_c and ρ_f may be critical). Thus, maximizing performance requires investigation of a much larger parameter space, which becomes difficult to plot and intuitively understand. Second, real-world materials do not allow arbitrary variations of material parameters (e.g., ρ, E, μ) with respect to one another; as a result, many discrete constraints must be imposed.

The preceding problem was effectively addressed through numerical optimization using mathematical analysis software (MATLAB 2018a, MathWorks, Natick, MA). A software routine was written that first allows designers to input an arbitrary set of available materials, as well as any mass, volume, and layer-thickness constraints relevant to their application. Next, the routine cycles through each possible pair of core and face materials and determines which pairs satisfy the assumptions of sandwich theory (i.e., $E_c << E_f$). For each pair of materials, the routine optimizes the geometry of the face, core, and individual laminae using a constrained nonlinear optimization algorithm ($fmincon$) in order to maximize the stiffness-to-mass, range-to-mass, and yield-to-mass ratios of the structure. The constraints are mass, volume, and layer-thickness constraints specified by the user, and the optimized parameters are geometric variables. The cost functions are simply the reciprocals of the performance-to-mass expressions for sandwich jamming structures derived in **SI: Theoretical Modeling**. Finally, for each of these performance metrics, the optimization routine determines the best-performing structure. A flow chart of the routine is shown in **Figure S5**.

A case study was used to illustrate the results of the routine. Four materials were input into the software routine (i.e., paper, low-density polyethylene (LDPE), polyurethane (PU) foam, and low-carbon steel), along with their material properties and minimum available thicknesses (**Table S3**). Arbitrary mass

and volume constraints were applied.

3.5 Design Example

Sandwich jamming structures may be useful in a range of applications, including assistive devices, vehicles, and deployable structures. We explored the first category by constructing a wrist orthosis with a sandwich jamming structure as a tunable-stiffness element. For patients with wrist injuries, a tunable-stiffness orthosis may reduce muscle activation during static weight-bearing tasks (e.g., carrying grocery bags), but enable flexibility during non-strenuous dynamic tasks (e.g., driving). A sandwich jamming structure presents a highly compelling tunable-stiffness structure for this application, as it not only has high stiffness-to-mass, range-to-mass, and yield-to-mass ratios, but is also thin, conformable, and rapidly activated. Thus, we built a sandwich-jamming wrist orthosis that was intended to facilitate isometric hold tasks when the structure was jammed, but allow full range-of-motion when unjammed.

The orthosis consisted of two separate non-slip fabric sleeves for both the hand and the arm. A sandwich jamming structure was attached to the palmar side of the hand via a hook-and-loop (i.e., Velcro) strap and was allowed to slide freely along the long axis of the arm within a low-friction pocket sewn on the proximal sleeve (**Figure 6A**). Electromyography (EMG) electrodes were placed on the skin above the flexor carpi ulnaris muscle to measure muscle activation (**Figure 6B**). This muscle was selected for two major reasons: 1) it is one of the dominant wrist flexor muscles, and 2) it is located superficially within the arm, facilitating placement of EMG electrodes. To place the electrodes, subjects were asked to flex their wrists, and the middle of the muscle belly was identified through palpation. Electrodes were placed directly above this location.

The optimization software routine was used to determine the materials and geometry of a high-performance sandwich jamming structure that satisfied specific mass and volume constraints; the sandwich jamming structure consisted of 6 layers of low-carbon steel, 30 layers of paper, and 6 layers of steel.

To evaluate the performance of the brace during weight-bearing activities, an isometric hold task was conducted on 9 human subjects (**Figure 6B-C**). The orthosis was fastened onto each subject, and electromyography (EMG) electrodes were located above the wrist flexor muscles. Each subject was requested to bend their elbow to 90 degrees and freely rest it on a flat surface. A weight was suspended from their hand, and the subject was requested to keep their wrist flat with minimal effort. Muscle activation was recorded. The test was conducted with 1) no orthosis, 2) the sandwich jamming brace in the inactive (i.e., unjammed) state, and 3) the brace in the active (i.e., jammed) state. For each subject, the EMG signal was normalized by the average EMG signal during a maximum voluntary contraction.

To evaluate the flexibility of the brace during non-weight-bearing activities, a range-of-motion test was also conducted (**Figure 6D**). During these tests, subjects were asked to flex and extend their wrists to the maximum angle that they still perceived as comfortable; the difference in angles was measured. The test was executed 3 times each for the no-brace and inactive conditions. A paired samples t-

test was conducted.

4 Results

4.1 Experimental Proof-of-Concept

Figure 2B shows force-deflection curves for a high-performing material configuration that consisted of steel face layers and paper core layers. (**Figure S1** shows analogous curves for an additional material configuration.) **Figure 2C** illustrates the general behavior of such structures.

For the steel-paper configuration, the jammed stiffness increased by up to a factor of 1850; furthermore, the maximum stiffness-to-mass, range-to-mass, and yield-to-mass improvement ratios were 560, 86, and 27, respectively. (**Table S1** provides the improvement ratios for additional material configurations.) The results demonstrated that by converting laminar jamming structures to sandwich jamming structures, performance improvements of 1 to 2 orders of magnitude could be readily achieved, motivating subsequent analysis and optimization.

4.2 Theoretical Modeling

Figure 3B-F provides contour maps that illustrate the functional dependence of the 3 improvement ratios (i.e., stiffness-to-mass improvement, range-to-mass improvement, and yield-to-mass improvement) on the non-dimensional design parameters (i.e., density ratio and thickness ratio) while imposing an equal-material constraint. As shown in the plots, the improvement ratios are nonlinear functions of the design parameters, with notable covariance. By converting a laminar jamming structure to a sandwich jamming structure, stiffness-to-mass and range-to-mass can both be readily improved by over 4 orders of magnitude, and yield-to-mass can improved by over 2 orders of magnitude. These improvements can be achieved by maximizing the total thickness ratio and friction ratio, and minimizing the density ratio, elastic modulus ratio, and layer thickness ratio.

4.3 Validation of Theoretical Model

Figure 4D-F compares theoretical predictions and finite element results. As illustrated, finite element simulations corroborated theoretical predictions with exceptional fidelity. In fact, the *minimum* coefficient of determination (R^2) between theoretical predictions and finite element results was greater than 0.99, indicating that the theoretical model exhibited excellent accuracy relative to a sophisticated computational reference.

Experimental results for a steel-paper sandwich jamming structure also closely supported theoretical predictions. In particular, for lower numbers of core layers (i.e., 20 and 25 layers), theoretically-predicted improvement ratios deviated from experimental results by no more than 13%. Numerical results for all numbers of layers and corresponding analyses are provided in **SI: Validation of Theoretical Model: Experimental Comparison**.

4.4 Optimization

The routine identified 5 material pairs (i.e., steel-paper, steel-LDPE, steel-foam, paper-foam, and LDPE-foam) that satisfied the assumptions of sandwich theory and recommended construction guidelines (i.e., $E_c >>$

E_f)[31, 25]. For the range-to-mass ratio, **Table 1** lists the best-performing sandwich structures for each material configuration, as well as their corresponding geometric properties. (**Table S4** and **Table S5** provide analogous data for the stiffness-to-mass and yield-to-mass ratios, respectively.)

In practical scenarios, mass and volume constraints may change frequently during prototyping. To provide designers with intuition about how a change of constraints can influence optimal geometries, the software routine can also generate contour maps that show how performance metrics vary with geometry, with constraints directly illustrated on the maps. **Figure 5** shows an example of these contour maps for a sandwich jamming structure consisting of steel face layers and paper core layers. To use these maps, the designer first chooses mass and/or volume constraints on the map. The designer then looks for the highest value of the performance metric (from the color bar) that lies to the left of the constraint lines. The optimal geometry is given by the x- and y-coordinates of this value, which denote the number of core and face layers, respectively. This process can be easily repeated for another set of mass and volume constraints as desired.

4.5 Design Examples

For the isometric hold task, **Figure 6E** shows muscle activation profiles (i.e., EMG signals) across the 3 evaluated conditions (i.e., no brace, inactive brace, and active brace) for a single representative subject, and **Figure 6F** depicts the average signal magnitudes across all 9 subjects. Paired t-tests indicated that the active and inactive conditions exhibited a statistically-significant difference ($p = 0.006$), demonstrating that the brace reduced musculoskeletal demand when activated; specifically, the average EMG signal magnitudes were reduced by a mean of 40.7% (standard error = 9.9%). On the other hand, the inactive and no-brace conditions did not exhibit a statistically-significant difference ($p = 0.70$), indicating that wearing the inactive brace did not affect baseline musculoskeletal demand.

For the range-of-motion test **(Figure 6D)**, the 2 evaluated conditions (i.e., no brace and inactive brace) exhibited a statistically significant difference ($p = 0.014$); however, subjects in the inactive state achieved an average of 94% of the angular range of motion that they achieved in the no-brace state (standard error = 1.8%). Thus, although range of motion was affected, it was essentially preserved.

5 Discussion

This paper introduced the concept of tunable jamming-based sandwich structures through experiments, models, and demonstrations. We first experimentally showed that simple sandwich jamming structures can achieve notably higher performance than laminar jamming structures. We then presented a theoretical model that describes how the performance-to-mass of laminar jamming structures can be improved by converting to a sandwich jamming architecture. This theoretical model explicitly relates critical design parameters (e.g., core-to-face thickness ratios) to performance metrics and was corroborated by finite-element simulations and experiments. Next, we provided an optimization tool that can identify the best-possible

sandwich jamming configuration given an arbitrary set of materials and mass-volume constraints. Finally, we demonstrated the utility of sandwich jamming structures by showing that a sandwich-jamming wrist orthosis can reduce muscle activation in isometric hold tasks when jammed, while allowing significant range of motion when unjammed. Collectively, our models, experiments, and demonstrations provide a full theoretical and empirical description of a novel structure that advances the state-of-the-art in tunable-stiffness mechanisms.

Our work offers four contributions. First, this paper proposes the concept of tunable jamming-based sandwich structures, which is one of the first explorations of tunable jamming-based composites in the literature. Previous studies have combined discrete granular and laminar jamming elements[35], combined discrete granular and fiber-based jamming elements[14], and integrated sensing and actuation components into jamming structures[36, 10], but did not investigate how to achieve high performance-to-mass, which is a trademark capability of composite materials and structures.

Second, we experimentally showed that our specific implementations of sandwich jamming structures were able to achieve exceptional mechanical properties. The structures outperformed the stiffness-, range-, and yield-to-mass of laminar jamming analogues by 1 to 2 orders of magnitude. Furthermore, these sandwich jamming structures well exceeded the performance of other tunable sandwich structures in the literature. Existing tunable sandwich structures have typically been constructed with one of the following features: 1) a core containing electrorheological fluid[26], 2) a core containing magnetorheological fluid[28], 3) a core containing shape-memory material[27, 30], and 4) facesheets that are electrostatically bonded to the core[29]. Among these structures, experimentally validated stiffness ranges are typically well below 2, and the highest range found in the literature was 18[29]. Our study experimentally demonstrated that a simple steel-paper sandwich jamming structure could achieve a stiffness range of 1850 in a lightweight form. In contrast to previous embodiments, our structure was low cost, could be rapidly activated, and did not require high voltages that could compromise safe interaction with humans.

As a third contribution, this paper provides a theoretical framework for designers to construct and optimize sandwich jamming structures to meet design requirements. Given an existing laminar jamming structure, the improvement ratios and associated contour maps inform designers precisely how the performance metrics of the structure (i.e., stiffness-to-mass, range-to-mass, and yield-to-mass) can be improved by adding a core and adjusting critical design parameters (i.e., thickness ratio, density ratio, elastic modulus ratio, layer number ratio, and friction ratio); these predictions show that improvement ratios of several orders of magnitude may be readily achievable. Moreover, the optimization code and associated contour maps allow designers to select an arbitrary set of face and core materials and rapidly determine the highest-performing structure that can meet their mass and volume constraints. Thus, the analysis enables designers to deterministically improve existing structures, as well as design optimal structures from the ground-up.

The design example comprises the final contribution of the paper, as it provides a feasible solution to a challenging engineering problem. In rehabilitation, previous efforts to determine whether wrist orthoses can reduce muscle activation have been inconclusive, with various studies showing moderately positive[37], negative[38], and neutral results[39]. Our study demonstrated that a sandwich-jamming orthosis reduced muscle activation by over 60% on a small population of participants, providing a compelling basis for further investigation. Moreover, in contrast to wrist orthoses that have previously been reported, the sandwich-jamming orthosis is highly tunable, allowing significant range of motion and causing no notable increase in muscle activation when inactive.

From a theoretical standpoint, future work will focus on deriving improvement ratios and contour maps for additional advantageous properties of sandwich jamming structures, such as damping, shear stiffness, damping range, and shear stiffness range (all with respect to mass). From an applied perspective, subsequent research will focus on making two design changes that may immediately improve the performance-to-mass of sandwich jamming structures even further: 1) using composite materials (e.g., carbon-fiber-reinforced polymers or fiberglass) as face layers, and 2) increasing the porosity of the core layers (e.g., by laser-cutting honeycomb patterns into the layers). Furthermore, to maximize portability of the sandwich jamming structures while preserving human safety, the sandwich jamming structures will be be activated with non-fluidic and non-electrostatic methods, such as tightening an elastic mesh around the layers[40]. Finally, we will apply our initial efforts to design and model mixed-media jamming structures (e.g., granular-laminar hybrids)[41, 19] to create mixed-media sandwich jamming structures with enhanced tunability and conformability. These improvements can augment the mechanical properties and utility of sandwich jamming structures, as well as lay a foundation for their commercial adoption in wearable robots, modern vehicles, and rapidly-deployable construction.

6 Conclusion

This paper proposed the novel concept of tunable, sandwich-based jamming structures. These structures were experimentally shown to have far higher performance-to-mass ratios than standard laminar jamming structures and existing tunable sandwich structures, as well as obvious versatility advantages over traditional sandwich structures. Theoretical models and finite element simulations were provided that allow designers to deterministically improve the performance-to-mass of laminar jamming structures by converting them to a sandwich architecture. A software routine was presented that also allowed designers to optimize sandwich jamming structures given arbitrary material, mass, and volume constraints. Finally, the utility of sandwich jamming structures was demonstrated through their integration into a wearable robotic device that significantly reduced muscle activation of human subjects in the on-state, while having negligible impact on activation in the off-state. Overall, sandwich jamming structures were shown to extend the performance boundaries of existing tunable-stiffness mechanisms, setting the stage for

ultra-light tunable-stiffness devices in the future. Subsequent work will focus on improving performance further through the incorporation of composite materials and portable jamming-activation mechanisms.

References

[1] B Vanderborght, A Albu-Schaeffer, A Bicchi, E Burdet, D.G Caldwell, R Carloni, M Catalano, O Eiberger, W Friedl, G Ganesh, M Garabini, M Grebenstein, G Grioli, S Haddadin, H Hoppner, A Jafari, M Laffranchi, D Lefeber, F Petit, S Stramigioli, N Tsagarakis, M Van Damme, R Van Ham, L.C Visser, and S Wolf. Variable impedance actuators: a review. *Robotics and Autonomous Systems*, 61(12):1601–1614, 2013.

[2] M Cianchetti, T Ranzani, G Gerboni, T Nanayakkara, K Althoefer, P Dasgupta, and A Menciassi. Soft robotics technologies to address shortcomings in today's minimally invasive surgery: the STIFF-FLOP approach. *Soft Robotics*, 1(2):122–131, 2014.

[3] M Manti, V Cacucciolo, and M Cianchetti. Stiffening in soft robotics: a review of the state of the art. *IEEE Robotics and Automation Magazine*, 23(3):93–106, 2016.

[4] YS Narang, JJ Vlassak, and RD Howe. Mechanically versatile soft machines through laminar jamming. *Advanced Functional Materials*, 28(17), 2018.

[5] JR Amend, E Brown, N Rodenberg, HM Jaeger, and H Lipson. A positive pressure universal gripper based on the jamming of granular material. *IEEE Transactions on Robotics*, 28(2):341–350, 2012.

[6] NG Cheng, MB Lobovsky, SJ Keating, AM Setapen, KI Gero, AE Hosoi, and KD Iagnemma. Design and analysis of a robust, low-cost, highly articulated manipulator enabled by jamming of granular media. In *Proceedings of the IEEE International Conference on Robotics and Automation (ICRA)*, pages 2922–2927, 2012.

[7] Y-J Kim, S Cheng, S Kim, and K Iagnemma. A novel layer jamming mechanism with tunable stiffness capability for minimally invasive surgery. *IEEE Transactions on Robotics*, 29(4):1031–1042, 2013.

[8] S Kawamura, T Yamamoto, D Ishida, T Ogata, Y Nakayama, O Tabata, and S Sugiyama. Development of passive elements with variable mechanical impedance for wearable robots. In *Proceedings of the IEEE International Conference on Robotics and Automation (ICRA)*, pages 248–253, 2002.

[9] S Follmer, D Leithinger, A Olwal, N Cheng, and H Ishii. Jamming user interfaces: programmable particle stiffness and sensing for malleable and shape-changing devices. In *Proceedings of the 25th Annual ACM Symposium on User Interface Software and Technology*, pages 519–528, 2012.

[10] J Ou, L Yao, D Tauber, J Steimle, R Niiyama, and H Ishii. jamSheets: thin interfaces with tunable stiffness enabled by layer jamming. In *Proceedings of the ACM International Conference on Tangible, Embedded, and Embodied Interactions*, 2014.

[11] AA Stanley and AM Okamura. Controllable surface haptics via particle jamming and pneumatics. *IEEE Transactions on Haptics*, 8(1):20–30, 2015.

[12] I Zubrycki and G Granosik. Novel haptic device using jamming principle for providing kinaesthetic feedback in glove-based control interface. *Journal of Intelligent & Robotic Systems*, 85:413–429, 2017.

[13] A Jiang, G Xynogalas, P Dasgupta, K Althoefer, and T Nanayakkara. Design of a variable stiffness flexible manipulator with composite granular jamming and membrane coupling. In *Proceedings of the IEEE/RSJ In-*

ternational Conference on Intelligent Robots and Systems (IROS), pages 2922–2927, 2012.

[14] E Thompson-Bean, O Steiner, and A McDaid. A soft robotic exoskeleton using granular jamming. In *Proceedings of the IEEE International Conference on Advanced Intelligent Mechatronics*, 2015.

[15] S Hauser, M Robertson, A Ijspeert, and J Paik. JammJoint: A variable stiffness device based on granular jamming for joint wearable support. *IEEE Robotics and Automation Letters*, 2(2):849–855, 2017.

[16] E Steltz, A Mozeika, J Rembisz, N Corson, and HM Jaeger. Jamming as an enabling technology for soft robotics. In *Proceedings of SPIE 7642, Electroactive Polymer Actuators and Devices (EAPAD)*, 2010.

[17] IK Kuder, AF Arrieta, WE Raither, and P Ermanni. Variable stiffness material and structural concepts for morphing applications. *Progress in Aerospace Sciences*, 63, 2013.

[18] YS Narang, A Degirmenci, JJ Vlassak, and RD Howe. Transforming the dynamic response of robotic structures and systems through laminar jamming. *IEEE Robotics and Automation Letters*, 3(2), 2018.

[19] N Vasios, YS Narang, B Aktas, RD Howe, and K Bertoldi. Numerical analysis of periodic laminar and fibrous media undergoing a jamming transition. *European Journal of Mechanics-A/Solids*, 75:322–329, 2019.

[20] M Bureau, T Keller, J Perry, R Velik, and JF Veneman. Variable stiffness structure for limb attachment. In *Proceedings of the IEEE International Conference on Rehabilitation Robotics (ICORR)*, 2011.

[21] Timothy Simon, Bruce Thomas, and Ross Smith. Low-profile jamming technology for medical rehabilitation. *IT Professional*, (5):28–34, 2015.

[22] RC Browning, JR Modica, R Kram, and A Goswami. The effects of adding mass to the legs on the energetics and biomechanics of walking. *Medicine and Science in Sports and Exercise*, 39, 2007.

[23] JC Watson, RC Payne, AT Chamberlain, RK Jones, and WI Sellers. The energetic costs of load-carrying and the evolution of bipedalism. *Journal of Human Evolution*, 54, 2008.

[24] JD Anderson. *Fundamentals of Aerodynamics*. MHS, 2010.

[25] D Zenkert. *Handbook of Sandwich Construction*. Engineering Materials Advisory Services Ltd., 1997.

[26] MV Gandhi, BS Thompson, and SB Choi. A new generation of innovative ultra-advanced intelligent composite materials featuring electro-rheological fluids: an experimental investigation. *Journal of Composite Materials*, 23, 1989.

[27] V Birman. Stability of functionally graded shape memory alloy sandwich panels. *Smart Materials and Structures*, 6, 1997.

[28] M Yalcintas and H Dai. Magnetorheological and electrorheological materials in adaptive structures and their performance comparison. *Smart Materials and Structures*, 8, 1999.

[29] A Bergamini, R Christen, B Maag, and M Motavalli. A sandwich beam with electrostatically tunable bending stiffness. *Smart Materials and Structures*, 15, 2006.

[30] P Butaud, E Foltte, and M Ouisse. Sandwich structures with tunable damping properties: On the use of shape memory polymer as viscoelastic core. *Composite Structures*, 153, 2016.

[31] D Zenkert. *Introduction to Sandwich Construction*. Engineering Materials Advisory Services Ltd., 1995.

[32] OA Bauchau and JI Craig. *Structural Analysis with Applications to Aerospace Structures*. Springer, 2009.

[33] FJ Plantema. *Sandwich Construction*. John Wiley & Sons, 1966.

[34] HG Allen. *Analysis and Design of Structural Sandwich Panels*. Pergamon Press, 1969.

[35] M Langer, E Amanov, and J Burgner-Kahrs. Stiffening sheaths for continuum robots. *Soft Robotics*, 5, 2018.

[36] L Yao, R Niiyama, J Ou, S Follmer, CD Silva, and H Ishii. PneUI: Pneumatically actuated soft composite materials for shape changing interfaces. In *Proceedings of the Annual ACM Symposium on User Interface Software and Technology*, 2013.

[37] CWS Jansen, S Olson, and SM Hasson. The effect of use of a wrist orthosis during functional activities on surface electromyography of the wrist extensors in normal subjects. *Journal of Hand Therapy*, 10, 1997.

[38] S Bulthaup, DJ Cipriani, and JJ Thomas. The effect of wrist orthoses on forearm muscle activity. *The American Journal of Occupational Therapy*, 53, 1999.

[39] L Johansson, G Bjring, and GM Hgg. The effect of wrist orthoses on forearm muscle activity. *Applied Ergonomics*, 35, 2004.

[40] JLC Santiago, IS Godage, P Gonthina, and ID Walker. Soft robots and kangaroo tails: modulating compliance in continuum structures through mechanical layer jamming. *Soft Robotics*, 2016.

[41] YS Narang. *Achieving Mechanical Versatility in Robots and Structures Through Laminar Jamming*. PhD thesis, Harvard University, 2018. Chapter 5.

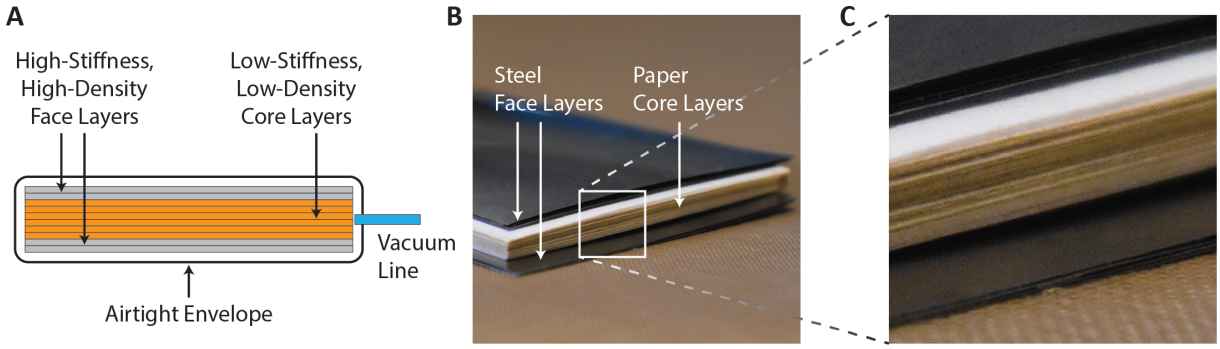

Figure 1: Concept and physical prototype of sandwich jamming structures. A) Conceptual diagram of a sandwich jamming structure. Face layers and core layers are enclosed in an airtight envelope connected to a vacuum line. When vacuum is applied, the structure exhibits a dramatic change in mechanical properties. B-C) Physical prototype of a steel-paper sandwich jamming structure. The layers within the airtight envelope are depicted.

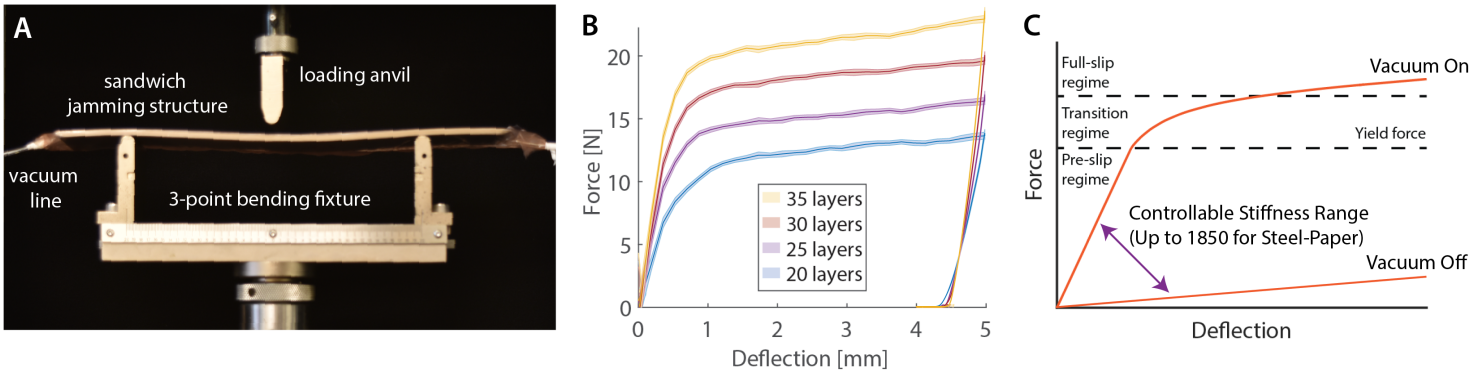

Figure 2: Fundamental behavior of sandwich jamming structures. A) Experimental setup to measure force-versus-deflection curves of sandwich jamming structures in 3-point bending. B) Force-versus-deflection curves of steel-paper sandwich jamming structures at $71kPa$ vacuum pressure during both loading and unloading. Curves are shown for different numbers of core layers. Each curve is a mean curve from 2 samples and 10 trials. Shaded error bars denote standard error. C) Conceptualized force-versus-deflection behavior during loading. As with standard laminar jamming structures[4], when vacuum is applied, the force-versus-deflection curves of sandwich jamming structures during loading consist of a high-stiffness regime (pre-slip), a yield force, a transition regime, and a low-stiffness regime (full-slip). (For simplicity, the unloading curve is not drawn.) When vacuum is not applied, the force-versus-deflection curves simply consist of a single low-stiffness regime. The difference in the slopes between the vacuum-on and vacuum-off states defines the stiffness range, which was measured to be up to 1850 for the steel-paper sandwich jamming structures in this study.

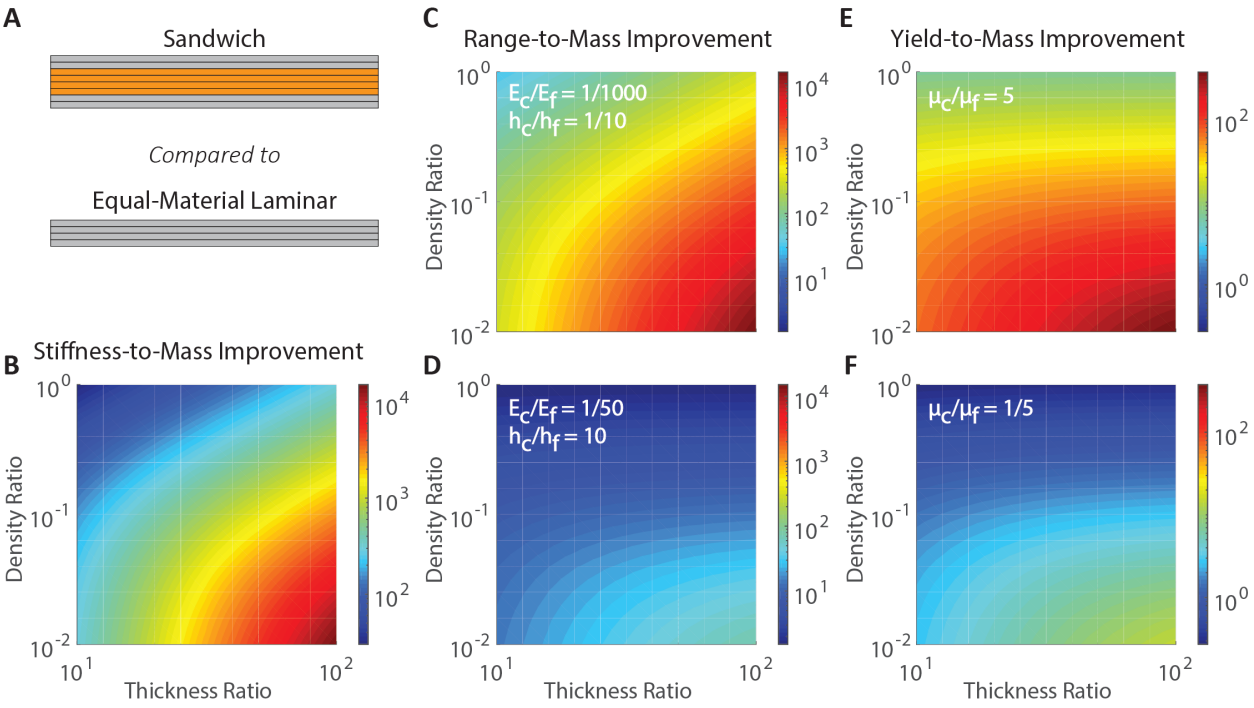

Figure 3: Contour maps of improvement ratios for a sandwich jamming structure compared to an equal-material laminar jamming structure. A) Conceptual diagrams of the compared jamming structures. B) Contour maps of improvement ratios. Each plot illustrates performance improvement as a function of density ratio ($\frac{\rho_c}{\rho_f}$) and total thickness ratio ($\frac{c}{f}$). Range-to-mass improvement is also a function of the product of the elastic modulus ratio and the square of the layer thickness ratio ($\frac{E_c}{E_f}(\frac{h_c}{h_f})^2$), and yield-to-mass improvement is also a function of the coefficient of friction ratio ($\frac{\mu_c}{\mu_f}$). Thus, 2 plots are provided for each of these performance metrics to show variation with these additional parameters. Design parameters are varied over a range representative of real-world limits. Note that both stiffness-to-mass and range-to-mass can be improved by 4 orders of magnitude, and yield-to-mass can be improved by 2 orders of magnitude.

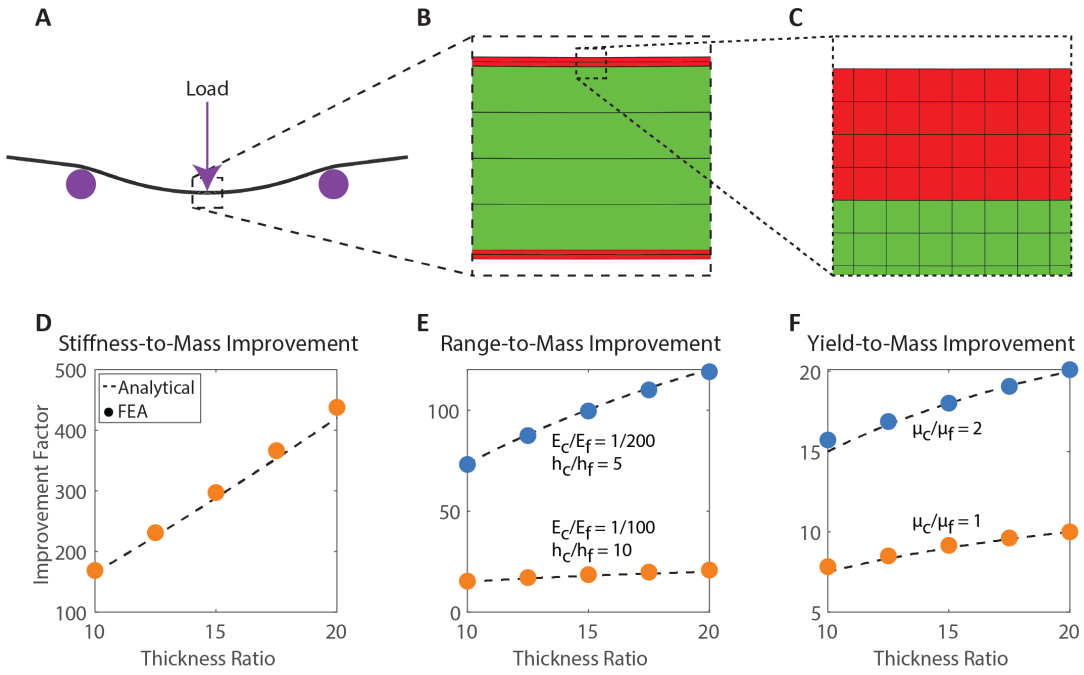

Figure 4: Comparison of theoretically-predicted improvement ratios to finite element results. Dashed lines denote theoretical predictions, and filled circles denote finite element results. The theoretically-predicted stiffness-to-mass, range-to-mass, and yield-to-mass improvement ratios were all closely corroborated by finite element values. The minimum coefficient of determination (R^2) between any theoretical and finite element data set was 0.992 for the yield-to-mass improvement ratios with $\frac{\mu_c}{\mu_f} = 2$.

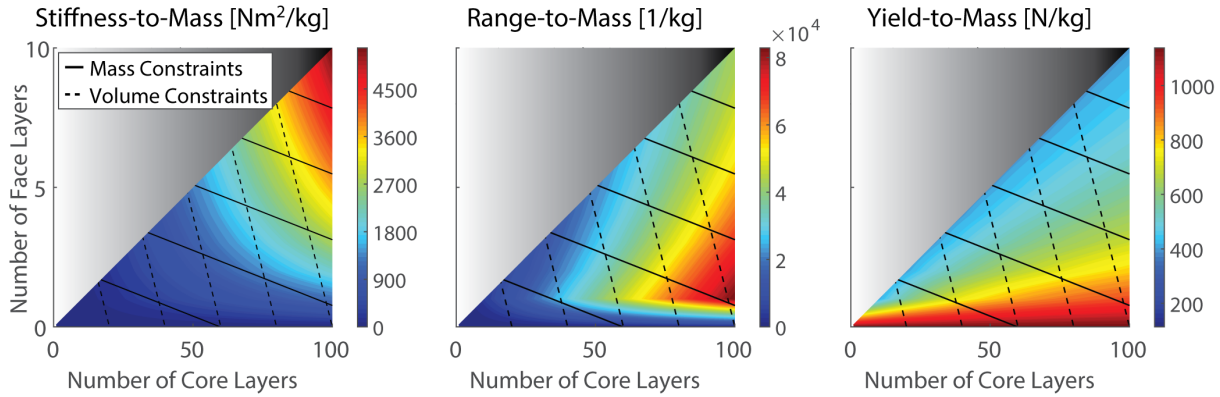

Figure 5: Contour maps for optimization of steel-paper sandwich structures. The plots illustrate the variation of optimal performance values and corresponding geometries (i.e., number of core and face layers) with applied constraints (i.e., maximum mass and/or volume). The mass and volume constraints are shown in solid and dashed lines, respectively, on each graph; from left-to-right, the mass constraints are $\{24, 48, 72, 96, 120\}g$, and the volume constraints are a maximum height of $\{2, 4, 6, 8, 10\}mm$. Grayscale regions do not satisfy a fundamental assumption of sandwich theory (i.e., $c >> f$), where c and f are the total thickness of the core and both faces, respectively.

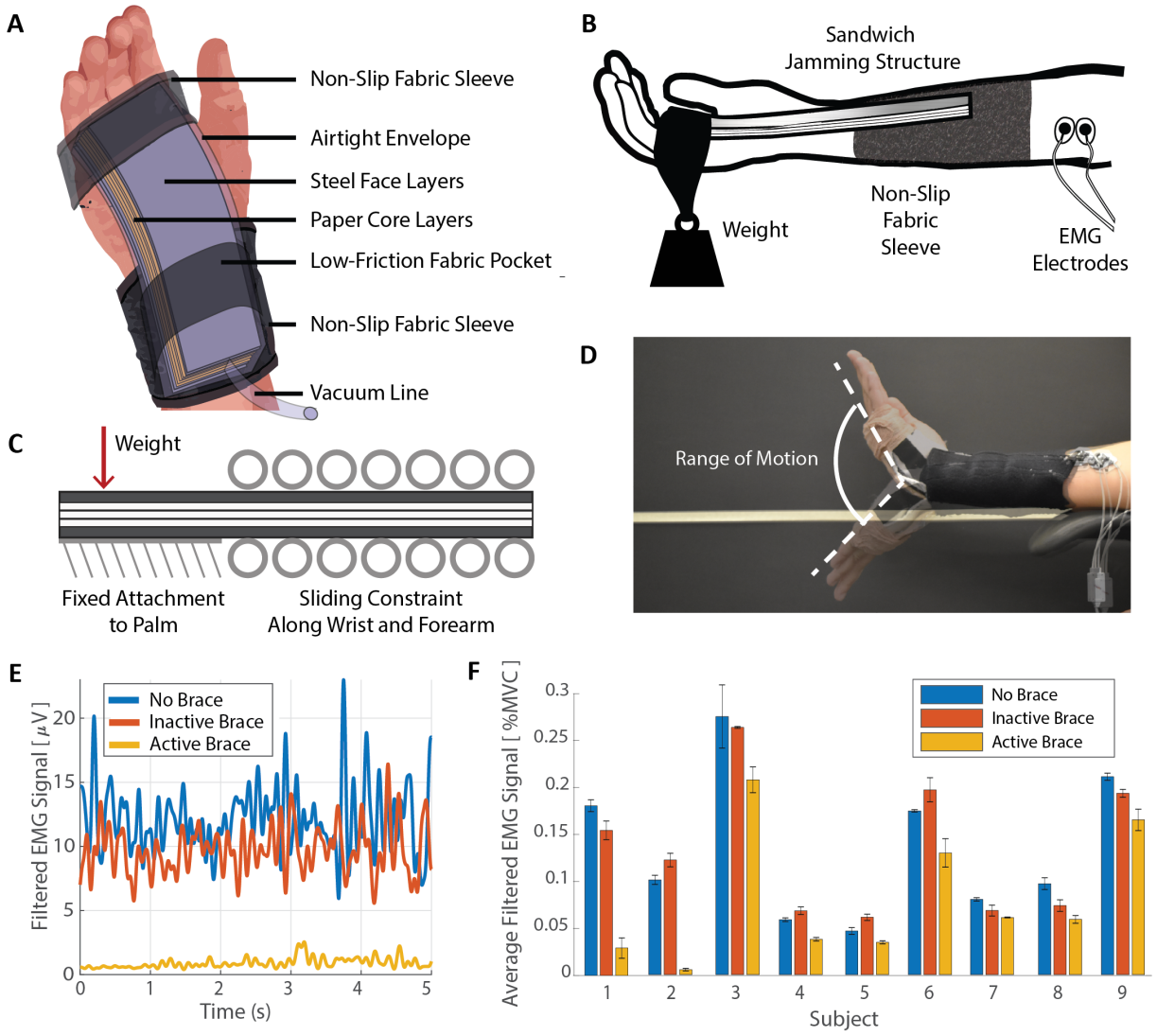

Figure 6: Overview of the sandwich-jamming wrist orthosis. A) Close-up diagram of orthosis. For simplicity, the hook-and-loop (i.e., Velcro) attachment on the distal fabric sleeve is not shown. B) Diagram of orthosis during isometric hold task. For simplicity, the hook-and-loop attachment and the low-friction fabric constraining the sandwich jamming structure are not depicted. C) Highly-simplified free-body diagram of sandwich jamming structure during isometric hold task. Note that during the task, the palm and wrist themselves were free-floating, whereas the forearm was supported by an armrest. D) Range-of-motion trials of a representative human subject in the no-brace and inactive conditions, respectively. Range of motion was largely preserved. E) Time-varying EMG signals for 1 representative subject during 1 trial. F) EMG signals for all 9 subjects, averaged over 3 trials and normalized with respect to their average EMG signals during maximum voluntary contractions. Error bars on the bar plot denote standard error.

Table 1: Results from the optimization case study for the range-to-mass ratio. Arbitrary mass constraints (total mass $\leq 47\ g$) and volume constraints (width $= 50\ mm$, length $= 100\ mm$, and total height $\leq 7.5\ mm$) were applied.

	Optimized Parameter				
Material Configuration	n_c	$h_c[m]$	n_f	$h_f[m]$	Range-to-mass $[\frac{1}{kg}]$
Steel-Paper	66	6.7e-3	2	5.0e-4	4.6e4
Steel-LDPE	63	6.4e-3	2	5.0e-4	4.5e4
Steel-Foam	8	7.0e-3	2	5.0e-4	6.8e4
Paper-Foam	8	6.8e-3	6	6.8e-4	5.2e5
LDPE-Foam	8	6.8e-3	6	6.8e-4	8.0e4

Supporting Information

1 Experimental Proof-of-Concept

1.1 Materials and Material Processing

- **Steel:** Stock consisted of 30 *cm* x 20 *cm* x 0.05 *mm* (12" x 8" x 0.002") low-carbon steel flat shim stock (9011K221, McMaster-Carr, Elmhurst, IL). Sheets were cut using a metal shear.
- **Paper:** Stock consisted of 28 *cm* x 43 *cm* x 0.1 *mm* (11" x 17" x 0.004") sheets of copy paper (Ultra White Multipurpose Copy Paper, HP Inc., Palo Alto, CA). Sheets were cut using a laser cutter (VLS4.60, Universal Laser Systems, Inc., Scottsdale, AZ).
- **Low-density polyethylene (LDPE):** Stock consisted of a 15 *m* x 90 *cm* x 0.1 *mm* (50 *ft* x 3 *ft* x 0.004") roll (8593K71, McMaster-Carr, Elmhurst, IL). Roll was manually cut using razor blades, as laser cutting produced rough edges.
- **Polyurethane (PU) foam:** Stock consisted of 30 *cm* x 30 *cm* x 0.8 *mm* (12" x 12" x $\frac{1}{32}$") sheets (86375K131, McMaster-Carr, Elmhurst, IL). Sheets were cut using a laser cutter (VLS4.60, Universal Laser Systems).

1.2 Sample Fabrication

The following samples were constructed:

- **Steel-paper:** 2 layers of steel, {20, 25, 30, 35} layers of paper, and 2 layers of steel, with dimensions of 30 *cm* x 2.5 *cm* (12" x 2"). Samples were enclosed in a tear-resistant TPE envelope (Stretchlon 800, Fibre Glast Developments Corp., Brookville, OH) with a thickness of 0.05 *mm* (2 *mil*).
- **Steel-LDPE:** 2 layers of steel, 20 layers of LDPE, and 2 layers of steel, with dimensions of 30 *cm* x 2.5 *cm* (12" x 2"). Samples were enclosed in a tear-resistant TPE envelope (Stretchlon 800, Fibre Glast Developments Corp.) with a thickness of 0.05 *mm* (2 *mil*). Only a single number of core layers was tested due to the difficulty of manually cutting the LDPE layers.
- **Paper-foam:** 2 layers of paper, {5, 6, 7, 8} layers of PU foam, and 2 layers of paper, with dimensions of 15 *cm* x 2.5 *cm* (5.75" x 2"). Samples were enclosed in a flexible TPE envelope (Stretchlon 200, Fibre Glast Developments Corp.) with a thickness of 0.04 *mm* (1.5 *mil*).

Two samples of each layer configuration were constructed. For each sample, the layers were stacked and enclosed within the corresponding TPE envelope. All 4 edges of the envelope were sealed using an impulse sealer (AIE-450FD, American International Electric Inc., City of Industry, CA). A small hole was cut in the envelope, and a thermoplastic polyurethane (TPU) tube with outer diameter of 3 *mm* (0.125") was inserted (TPU1-2N,

Eldon-James Corp., Denver, CO). Polytetrafluoroethylene (PTFE) thread seal tape was then wrapped around the interface between the TPU tube and the TPE envelope to ensure an airtight seal. Photographs and videos of an equivalent fabrication process for standard laminar jamming structures have been published to the Soft Robotics Toolkit, an open-access educational website[1].

1.3 Sample Testing

All samples were tested on a 3-point bending fixture (Instron 2810-400, Illinois Tool Works, Norwood, MA) in a universal materials testing device (Instron 5566, Illinois Tool Works) with a loading anvil attached to a load cell with a 100 N force capacity (Instron 2525-807, Illinois Tool Works).

Prior to each test, the supporting anvils were separated by 15 cm, 15 cm, and 9 cm for the steel-paper, steel-LDPE, and paper-foam samples, respectively, in order to prevent them from bulging or sagging in the unjammed state. The samples were connected to a vacuum source that was regulated to 71 kPa (21 $inHg$) using a manual vacuum regulator (EW-07061-30, Cole-Parmer, Vernon Hills, IL). The samples were then flattened using a rolling pin in order to remove large air pockets.

To ensure that the deflection of the samples was measured with respect to initial contact, the samples were preloaded at 5 $\frac{mm}{min}$ to a nominal force value of 0.1 N; at this point, deflection measurements were zeroed. The samples were then loaded at 20 $\frac{mm}{min}$ to a maximum deflection of 5 mm, 2 mm, and 5 mm for the steel-paper, steel-LDPE, and paper-foam samples, respectively. They were unloaded at the same rate. Force and deflection values were recorded during loading and unloading. After each test, the samples were released from vacuum and gently flexed to facilitate their return to atmospheric pressure. Tests were repeated 5 times per sample.

1.4 Data Processing

Raw data were imported into mathematical analysis software (MATLAB 2018a, MathWorks, Natick, MA). For each layer configuration, data from both samples and all trials were averaged to produce a mean force-versus-deflection curve. Error bars corresponding to standard error were illustrated at each point along the curve using the *shadedErrorBar* package[2]. Yield forces were determined by manually estimating the end of the initial linear regime. For each trial, the maximum stiffness was determined by finding a line of best fit to the unloading curve using the least squares method. Note that the unloading curve was used rather than the loading curve due to its enhanced repeatability. The slopes were averaged across all trials to compute the stiffness for each sandwich structure.

1.5 Additional Data

Figure S1 shows experimental force-versus-deflection data for the paper-foam sandwich jamming structures. Furthermore, **Table S1** shows a comparison of improvement ratios extracted from force-versus-deflection curves for all examined material configurations.

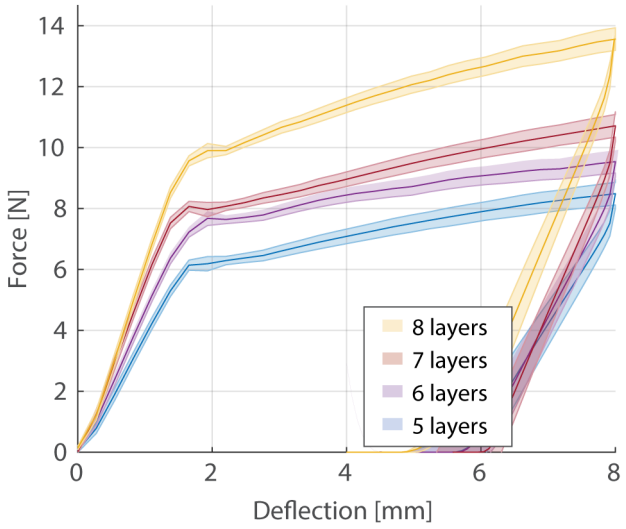

Figure S1: Force-versus-deflection curves for paper-foam sandwich jamming structures in 3-point bending at 71 kPa vacuum pressure. Curves are shown for different numbers of core layers. Each curve is a mean curve from 2 samples and 10 trials; shaded error bars delimit ± 1 standard deviation.

Table S1: Performance-to-mass improvements for 3 material configurations examined during the experimental proof-of-concept of sandwich jamming structures. Recall from **SI: Sample Fabrication**, 4 different numbers of core layers were tested, whereas for the steel-LDPE configuration, a single number of core layers (i.e, 20) was tested. For each maximum improvement ratio, the corresponding number of layers is listed. Note that steel-paper sandwich jamming structures had by far the best stiffness-to-mass and yield-to-mass improvement ratios, as well as the second-best range-to-mass improvement ratio.

Material Configuration	Maximum Stiffness-to-Mass Improvement	# of Layers	Maximum Range-to-Mass Improvement	# of Layers	Maximum Yield-to-Mass Improvement	# of Layers
Steel-Paper	560	35	86	35	27	35
Steel-LDPE	18	20	132	20	0.7	20
Paper-Foam	38	8	16	8	4.2	8

2 Theoretical Modeling

2.1 Derivation of Improvement Ratios

2.1.1 Stiffness, Range, and Yield of a Single-Material Laminar Jamming Structure

For a single-material laminar jamming structure with a rectangular cross-section in the jammed state, the bending stiffness is

$$k_b = EI = \frac{EbH^3}{12} \tag{1}$$

where E is the elastic modulus, I is the second moment of area (also referred to as the "area moment of inertia"), b is the width of the structure, and H is the total thickness of the structure[3].

The range is

$$r = n^2 \tag{2}$$

where n is the number of layers[3].

The yield force is

$$F_{crit} = \frac{4bH\mu P}{3} \tag{3}$$

where μ is the coefficient of friction of the layers and P is the vacuum pressure (i.e., the absolute pressure applied to the structure below ambient pressure)[3].

2.1.2 Stiffness, Range, and Yield of a Sandwich Jamming Structure

For a cohesive sandwich structure, the bending stiffness is

$$k_b = \frac{E_c c^3}{12} + \frac{E_f(\frac{f}{2})(c+\frac{f}{2})^2}{2} + \frac{E_f(\frac{f}{2})^3}{6} \tag{4}$$

where E_c and E_f are the elastic moduli of the core and face, respectively; and c and f are the total thickness of the core and both faces, respectively[4]. If the faces are thin (i.e., $f << c$) and the core is compliant (i.e., $E_c << E_f$), then the bending stiffness can be approximated as

$$k_b \approx E_f b\frac{\frac{f}{2}(c+\frac{f}{2})^2}{2} = E_f b\frac{4c^2f + 4cf^2 + f^3}{16} \tag{5}$$

To calculate the range, we first compute the jammed bending stiffness. This stiffness is simply equal to that of a cohesive sandwich structure given in (5). Assume that the sandwich jamming structure consists of n_c core layers, each of height h_c, and n_f total face layers, each of height h_f. Thus, $c = n_c h_c$ and $f = n_f h_f$. Substituting these expressions into (5), the jammed bending stiffness can be written as

$$k_b^{jam} \approx E_f b\frac{4(n_c h_c)^2 f + 4(n_c h_c)(n_f h_f)^2 + (n_f h_f)^3}{16} \tag{6}$$

Next, we calculate the unjammed bending stiffness. This stiffness is simply equal to the sum of the individual stiffnesses of all the layers. Thus, the unjammed bending stiffness is

$$k_b^{unjam} = b\frac{E_c n_c h_c^3 + E_f n_f h_f^3}{12} \tag{7}$$

The range is the ratio of the jammed to unjammed bending stiffnesses. Thus, the range is

$$r = E_f \frac{12(n_c h_c)^2(n_f h_f) + 12(n_c h_c)(n_f h_f)^2 + 3(n_f h_f)^3}{4(E_c n_c h_c^3 + E_f n_f h_f^3)} \tag{8}$$

The yield force is calculated by equating the maximum longitudinal shear stress with the maximum allowable shear stress. Again, for thin faces and a compliant core, the shear stress is approximately negligible in the faces and uniformly distributed in the core. The maximum longitudinal shear stress is thus

$$\tau_{max} = \frac{V}{A} = \frac{V}{bc} \tag{9}$$

where V is the resultant shear and A is the cross-sectional area. In 3-point bending, $V = \frac{F}{2}$, where F is the applied load. Thus,

$$\tau_{max} = \frac{F}{2bc} \tag{10}$$

The maximum allowable shear stress is simply

$$\tau_{allow} = \mu_c P \tag{11}$$

where μ_c is the coefficient of friction of the core material. Equating (10) and (11) and solving for F, the yield force is

$$F_{crit} = 2bc\mu_c P \tag{12}$$

Note that if $\mu_{cf} < \mu_c$, where μ_{cf} is the coefficient of friction between the core and the face, then μ_{cf} should be used in the preceding expression, as the structure will begin to slip at the interfaces between the core and face.

2.1.3 Equal-Material Improvement Ratios

Bending Stiffness: The bending stiffness of a sandwich jamming structure is

$$k_b \approx E_f b\frac{4c^2 f + 4cf^2 + f^3}{16} \tag{13}$$

The mass is

$$m = \rho_c bcL + \rho_f bfL \tag{14}$$

where m is the mass, ρ_c is the density of the core material, ρ_f is the density of the face material, and L is the length. Thus, the stiffness-to-mass ratio of a sandwich jamming structure is

$$\frac{k_b}{m} \approx E_f \frac{4c^2 f + 4cf^2 + f^3}{16L(\rho_c c + \rho_f f)} \tag{15}$$

A single-material jamming structure composed of just the face material (i.e., an equal-material jamming structure) has thickness f. Thus, the bending stiffness of an equal-material jamming structure is

$$k_b = E_f \frac{bf^3}{12} \tag{16}$$

The mass is

$$m = \rho_f bfL \tag{17}$$

Thus, the stiffness-to-mass ratio is

$$\frac{k_b}{m} = E_f \frac{f^2}{12L\rho_f} \tag{18}$$

Thus, the ratio of the stiffness-to-mass-ratios of a sandwich jamming structure and that of an equal-material jamming structure is

$$\left(\frac{k_b}{m}\right)^* = \frac{12(\frac{c}{f})^2 + 12\frac{c}{f} + 3}{4(\frac{\rho_c}{\rho_f}\frac{c}{f} + 1)} \tag{19}$$

Range: The range of a sandwich jamming structure is

$$r = E_f \frac{12(n_c h_c)^2(n_f h_f) + 12(n_c h_c)(n_f h_f)^2 + 3(n_f h_f)^3}{4(E_c n_c h_c^3 + E_f n_f h_f^3)} \tag{20}$$

The mass is

$$m = \rho_c bcL + \rho_f bfL \tag{21}$$

Thus, the range-to-mass ratio is

$$\frac{r}{m} = E_f \frac{12(n_c h_c)^2(n_f h_f) + 12(n_c h_c)(n_f h_f)^2 + 3(n_f h_f)^3}{4bL(E_c n_c h_c^3 + E_f n_f h_f^3)(\rho_c c + \rho_f f)} \tag{22}$$

The range of an equal-material jamming structure is

$$r = n_f^2 \tag{23}$$

where n_f is the number of layers in the face of the sandwich jamming structure.

The mass is

$$m = \rho_f bfL \tag{24}$$

Thus, the range-to-mass ratio is

$$\frac{r}{m} = \frac{n_f^2}{bL\rho_f f} = \frac{n_f}{bL\rho_f h_f} \tag{25}$$

Thus, the ratio of the range-to-mass-ratios of a sandwich jamming structure and that of an equal-material jamming structure can be written as

$$\left(\frac{r}{m}\right)^* = \frac{12(\frac{c}{f})^2 + 12\frac{c}{f} + 3}{4(\frac{E_c}{E_f}(\frac{h_c}{h_f})^2\frac{c}{f} + 1)(\frac{\rho_c}{\rho_f}\frac{c}{f} + 1)} \tag{26}$$

Yield: The yield of a sandwich jamming structure is

$$F_{crit} = 2bc\mu_c P \tag{27}$$

The mass is

$$m = \rho_c bcL + \rho_f bfL \tag{28}$$

Thus, the yield-to-mass ratio is

$$\frac{F_{crit}}{m} = \frac{2\mu_c P}{L(\rho_c + \rho_f(\frac{c}{f})^{-1})} \tag{29}$$

The yield of an equal-material jamming structure is

$$F_{crit} = \frac{4bf\mu_f P}{3} \tag{30}$$

The mass is

$$m = \rho_f bfL \tag{31}$$

Thus, the yield-to-mass ratio is

$$\frac{F_{crit}}{m} = \frac{4\mu_f P}{3L\rho_f} \tag{32}$$

Thus, the ratio of the yield-to-mass-ratios of a sandwich jamming structure and that of an equal-material jamming structure is

$$\left(\frac{F_{crit}}{m}\right)^* = \frac{3}{2}\frac{\mu_c}{\mu_f}\frac{\frac{c}{f}}{\frac{\rho_c}{\rho_f}\frac{c}{f}+1} \tag{33}$$

2.1.4 Equal-Mass Improvement Ratios

Because the masses are the same, the ratio of stiffness-to-mass ratios is simply equal to the ratio of stiffness, and so on for the other performance metrics.

Bending Stiffness: The bending stiffness of a sandwich jamming structure is

$$k_b \approx E_f b\frac{4c^2 f + 4cf^2 + f^3}{16} \tag{34}$$

The mass of the sandwich jamming structure is the same as that of the equal-mass jamming structure. Thus,

$$\rho_c bcL + \rho_f bfL = \rho_f bHL \tag{35}$$

$$H = \frac{\rho_c}{\rho_f}c + f \tag{36}$$

where H is the total thickness of the structure. Thus, the stiffness of an equal-mass jamming structure is

$$k_b = E_f\frac{b(\frac{\rho_c}{\rho_f}c+f)^3}{12} = E_f b\frac{(\frac{\rho_c}{\rho_f})^3c^3 + 3(\frac{\rho_c}{\rho_f})^2c^2 f + 3\frac{\rho_c}{\rho_f}cf^2 + f^3}{12} \tag{37}$$

Thus, the ratio of the stiffness-to-mass-ratios of a sandwich jamming structure and that of an equal-mass jamming structure is

$$\left(\frac{k_b}{m}\right)^* = \frac{12(\frac{c}{f})^2 + 12\frac{c}{f} + 3}{4(\frac{\rho_c}{\rho_f})^3(\frac{c}{f})^3 + 12(\frac{\rho_c}{\rho_f})^2(\frac{c}{f})^2 + 12\frac{\rho_c}{\rho_f}\frac{c}{f} + 4} \tag{38}$$

Range: The range of a sandwich jamming structure is

$$r = E_f \frac{12(n_c h_c)^2(n_f h_f) + 12(n_c h_c)(n_f h_f)^2 + 3(n_f h_f)^3}{4(E_c n_c h_c^3 + E_f n_f h_f^3)} \tag{39}$$

Again, the thickness of an equal-mass jamming structure is

$$H = \frac{\rho_c}{\rho_f} c + f \tag{40}$$

Thus, the range of an equal-mass jamming structure is

$$r = n_f^2 = \left(\frac{H}{h_f}\right)^2 = \frac{(\frac{\rho_c}{\rho_f})^2(n_c h_c)^2 + 2\frac{\rho_c}{\rho_f}(n_c h_c)(n_f h_f) + (n_f h_f)^2}{h_f^2} \tag{41}$$

where it is assumed that h_f for the equal-mass jamming structure is the same as that for the sandwich jamming structure.

Thus, the ratio of the range-to-mass-ratios of a sandwich jamming structure and that of an equal-mass jamming structure is

$$\left(\frac{r}{m}\right)^* = \frac{12(\frac{c}{f})^2 + 12\frac{c}{f} + 3}{4(\frac{E_c}{E_f}(\frac{h_c}{h_f})^2\frac{c}{f} + 1)\left((\frac{\rho_c}{\rho_f})^2(\frac{c}{f})^2 + 2\frac{\rho_c}{\rho_f}\frac{c}{f} + 1\right)} \tag{42}$$

Yield: The yield of a sandwich jamming structure is

$$F_{crit} = 2bc\mu_c P \tag{43}$$

Again, the thickness of an equal-mass jamming structure is

$$H = \frac{\rho_c}{\rho_f} c + f \tag{44}$$

Thus, the yield of an equal-mass jamming structure is

$$F_{crit} = \frac{4b(\frac{\rho_c}{\rho_f} c + f)\mu_f P}{3} \tag{45}$$

Thus, the ratio of the yield-to-mass-ratios of a sandwich jamming structure and that of an equal-mass jamming structure is

$$\left(\frac{F_{crit}}{m}\right)^* = \frac{3}{2}\frac{\mu_c}{\mu_f}\frac{\frac{c}{f}}{\frac{\rho_c}{\rho_f}\frac{c}{f} + 1} \tag{46}$$

2.1.5 Equal-Volume Improvement Ratios

Bending Stiffness: The stiffness-to-mass ratio of a sandwich jamming structure is

$$\frac{k_b}{m} \approx E_f \frac{4c^2 f + 4cf^2 + f^3}{16L(\rho_c c + \rho_f f)} \tag{47}$$

The volume of the sandwich jamming structure is the same as that of the equal-volume jamming structure. Thus,

$$H = c + f \tag{48}$$

Thus, the stiffness-to-mass ratio of an equal-volume jamming structure is

$$\frac{k_b}{m} = E_f \frac{(c+f)^2}{12L\rho_f} = E_f \frac{c^2 + 2cf + f^2}{12L\rho_f} \tag{49}$$

Thus, the ratio of the stiffness-to-mass-ratios of a sandwich jamming structure and that of an equal-volume jamming structure is

$$\left(\frac{k_b}{m}\right)^* = \frac{12(\frac{c}{f})^2 + 12\frac{c}{f} + 3}{4\left((\frac{c}{f})^2 + 2\frac{c}{f} + 1\right)(\frac{\rho_c}{\rho_f}\frac{c}{f} + 1)} \tag{50}$$

Range: The range-to-mass ratio of a sandwich jamming structure is

$$\frac{r}{m} = E_f \frac{12(n_c h_c)^2 (n_f h_f) + 12(n_c h_c)(n_f h_f)^2 + 3(n_f h_f)^3}{4bL(E_c n_c h_c^3 + E_f n_f h_f^3)(\rho_c c + \rho_f f)} \tag{51}$$

Again,

$$H = c + f \tag{52}$$

Thus, the range-to-mass ratio of an equal-volume jamming structure is

$$\frac{r}{m} = \frac{n_f^2}{bL\rho_f(c+f)} \tag{53}$$

Thus, the ratio of the range-to-mass-ratios of a sandwich jamming structure and that of an equal-volume jamming structure is

$$\frac{(12(\frac{c}{f})^2 + 12\frac{c}{f} + 3)(\frac{c}{f} + 1)}{4(\frac{E_c}{E_f}(\frac{h_c}{h_f})^2 \frac{c}{f} + 1)(\frac{\rho_c}{\rho_f}\frac{c}{f} + 1)} \tag{54}$$

Yield: The yield-to-mass ratio of a sandwich jamming structure is

$$\frac{F_{crit}}{m} = \frac{2\mu_c P}{L(\rho_c + \rho_f(\frac{c}{f})^{-1})} \tag{55}$$

The yield-to-mass ratio of an equal-volume jamming structure is

$$\frac{F_{crit}}{m} = \frac{4\mu_f P}{3L\rho_f} \tag{56}$$

Note that this expression does not depend on the height of the structure, as both the yield and the mass are proportional to the height. Thus, the ratio of the yield-to-mass-ratios of a sandwich jamming structure and that of an equal-volume jamming structure is

$$\left(\frac{F_{crit}}{m}\right)^* = \frac{3}{2}\frac{\mu_c}{\mu_f}\frac{\frac{c}{f}}{\frac{\rho_c}{\rho_f}\frac{c}{f}+1} \tag{57}$$

which is the same as the previous expressions.

2.1.6 Summary of Formulae

The final results from above are collected and rewritten below in comparable forms.

For equal material,

$$\left(\frac{k_b}{m}\right)^* = \frac{12(\frac{c}{f})^2+12\frac{c}{f}+3}{4(\frac{\rho_c}{\rho_f}\frac{c}{f}+1)} \tag{58}$$

$$\left(\frac{r}{m}\right)^* = \frac{12(\frac{c}{f})^2+12\frac{c}{f}+3}{4(\frac{E_c}{E_f}(\frac{h_c}{h_f})^2\frac{c}{f}+1)(\frac{\rho_c}{\rho_f}\frac{c}{f}+1)} \tag{59}$$

$$\left(\frac{F_{crit}}{m}\right)^* = \frac{3}{2}\frac{\mu_c}{\mu_f}\frac{\frac{c}{f}}{\frac{\rho_c}{\rho_f}\frac{c}{f}+1} \tag{60}$$

For equal mass,

$$\left(\frac{k_b}{m}\right)^* = \frac{12(\frac{c}{f})^2+12\frac{c}{f}+3}{4(\frac{\rho_c}{\rho_f}\frac{c}{f}+1)^3} \tag{61}$$

$$\left(\frac{r}{m}\right)^* = \frac{12(\frac{c}{f})^2+12\frac{c}{f}+3}{4(\frac{E_c}{E_f}(\frac{h_c}{h_f})^2\frac{c}{f}+1)(\frac{\rho_c}{\rho_f}\frac{c}{f}+1)^2} \tag{62}$$

$$\left(\frac{F_{crit}}{m}\right)^* = \frac{3}{2}\frac{\mu_c}{\mu_f}\frac{\frac{c}{f}}{\frac{\rho_c}{\rho_f}\frac{c}{f}+1} \tag{63}$$

For equal volume,

$$\left(\frac{k_b}{m}\right)^* = \frac{12(\frac{c}{f})^2+12\frac{c}{f}+3}{4\left((\frac{c}{f})^2+2\frac{c}{f}+1\right)(\frac{\rho_c}{\rho_f}\frac{c}{f}+1)} \tag{64}$$

$$\left(\frac{r}{m}\right)^* = \frac{(12(\frac{c}{f})^2+12\frac{c}{f}+3)(\frac{c}{f}+1)}{4(\frac{E_c}{E_f}(\frac{h_c}{h_f})^2\frac{c}{f}+1)(\frac{\rho_c}{\rho_f}\frac{c}{f}+1)} \tag{65}$$

$$\left(\frac{F_{crit}}{m}\right)^* = \frac{3}{2}\frac{\mu_c}{\mu_f}\frac{\frac{c}{f}}{\frac{\rho_c}{\rho_f}\frac{c}{f}+1} \tag{66}$$

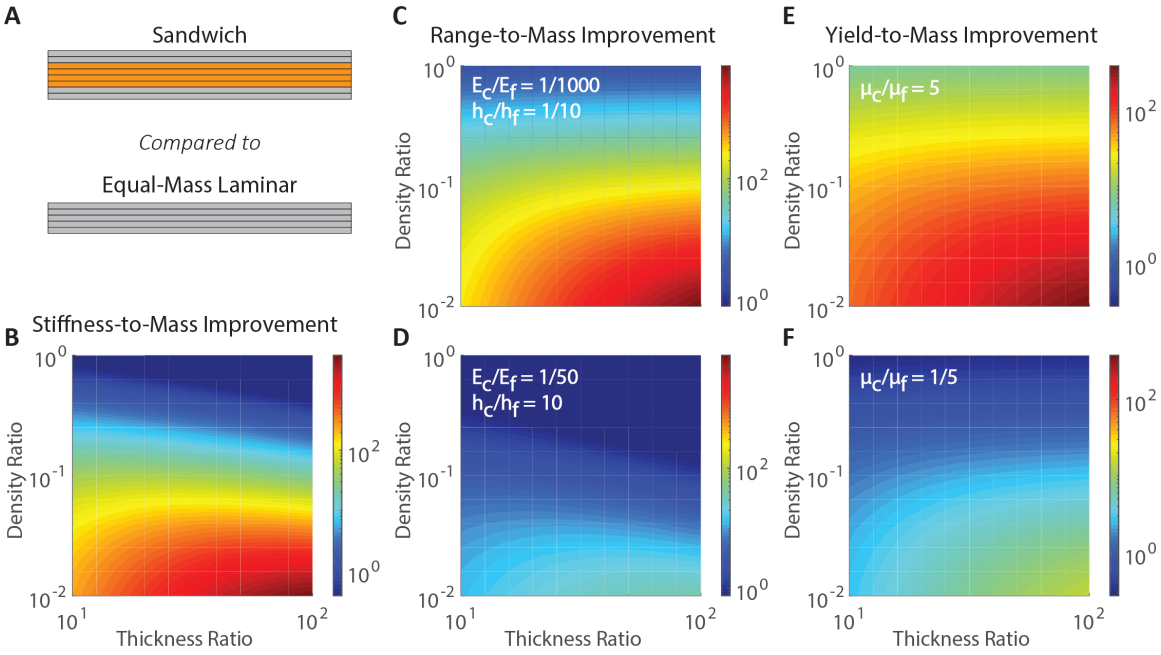

Figure S2: Contour maps illustrating improvement ratios of sandwich jamming structures compared to equal-mass laminar jamming structures. A) Diagram of an equal-mass laminar jamming structure. B-F) Contour maps illustrating improvement ratios of sandwich jamming structures compared to equal-mass laminar jamming structures. Note that over the examined range of parameters, stiffness-to-mass and range-to-mass can be improved by almost 3 orders of magnitude, whereas yield-to-mass can be improved by 2 orders of magnitude.

Note that although the stiffness-to-mass improvement ratios depend only on the density ratio and the total thickness ratio, the range-to-mass and yield-to-mass improvement ratios depend on additional non-dimensional parameters. The range-to-mass improvement ratio also depends on $\frac{E_c}{E_f}(\frac{h_c}{h_f})^2$, and the yield-to-mass improvement ratio depends on $\frac{\mu_c}{\mu_f}$.

2.2 Contour Maps for Equal-Mass and Equal-Volume Comparisons

Analogous to the contour maps provided in **Figure 3** for the equal-material comparison, contour maps for the equal-mass and equal-volume comparisons are provided in **Figure S2** and **Figure S3**, respectively.

3 Validation of Theoretical Model

3.1 Finite Element Analysis

3.1.1 Procedures and Parameters

To corroborate the predictions of the theoretical model, finite element simulations were conducted using commercial simulation software (Abaqus 2017, Dassault Systèmes, Vélizy-Villacoublay, France). Each layer was defined as a 2-dimensional body where the length and

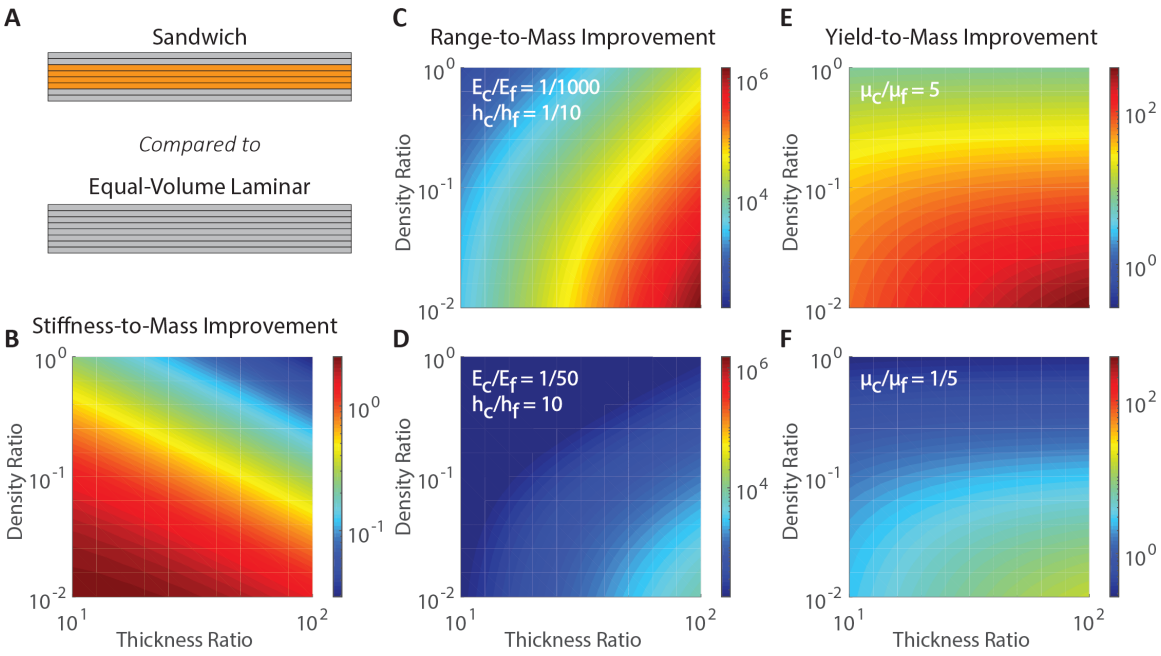

Figure S3: Contour maps illustrating improvement ratios of sandwich jamming structures compared to equal-volume laminar jamming structures. A) Diagram of an equal-volume laminar jamming structure. B-F) Contour maps illustrating improvement ratios of sandwich jamming structures compared to equal-volume laminar jamming structures. Note that over the examined range of parameters, range-to-mass can be improved by 6 orders of magnitude, whereas yield-to-mass can be improved by 2 orders of magnitude.

Table S2: Dimensional and material parameters used in the finite element simulations. Brackets denote a set of multiple discrete values that were simulated. Note that c and f were not directly varied, but are simply computed here by the relations $c = n_c h_c$ and $f = n_f h_f$. Also note that in the set of simulations for which $h_c = 0.125$ (i.e., the second row of the table), the number of core values are doubled in order to ensure that the thickness ratio $\frac{c}{f}$ has a consistent range over all simulations.

n_c	n_f	h_c $[mm]$	h_f $[mm]$	c $[mm]$	f $[mm]$	E_c $[MPa]$	E_f $[MPa]$	μ_c	μ_f
{4,5,6,7,8}	4	0.25	0.025	{1,1.25,1.5,1.75,2}	0.1	100	1e4	0.25	0.25
{8,10,12,14,16}	4	0.125	0.025	{1,1.25,1.5,1.75,2}	0.1	50	1e4	0.25	0.25
{4,5,6,7,8}	4	0.25	0.025	{1,1.25,1.5,1.75,2}	0.1	100	1e4	0.5	0.25

thickness were directly modeled and the width was prescribed. For all layers, $L = 150\ mm$ and $w = 1\ mm$, where L is the length and w is the width. Additionally, $\nu_c = \nu_f = 0.25$, where ν_c and ν_f are the Poisson's ratios of the core and face material, respectively.

Frictional contact with a *general contact* formulation was prescribed at the interfaces between the layers. To mitigate elastic slip, a strict elastic slip tolerance of $5 * 10^{-5}$ was prescribed. A static implicit solver was selected, and large-deformation analysis was enabled. A uniform mesh of square plane-stress elements with reduced integration (CPS4R) was used, with 2 elements across the thickness of each face layer (**Figure 4C**). A mesh refinement study was conducted to ensure that a finer mesh was not necessary.

The model was loaded and supported in 3-point bending (**Figure 4A**). For support, $\delta_{supp} = 100\ mm$, where δ_{supp} is the distance between the support points. For loading, in a first step, pressure (equal to vacuum pressure) was applied as a ramp to all outer surfaces of the model. In a second step, a vertical displacement boundary condition was applied as a ramp to the center node of the topmost surface with $\delta_{load} = 10\ mm$, where δ_{load} is the maximum loading distance. Automatic timestepping was enabled.

Dimensional and material parameters were varied in order to sufficiently corroborate the theoretical results over a wide range of the parameter space. The specific values of these parameters are given in **Table S2**. For each simulation, the vertical reaction force and displacement were extracted at the loading point. Corresponding force-versus-deflection curves are given in **Figure S4**.

3.1.2 A Note on the Comparison to Theoretical Predictions

Stiffnesses were derived from the finite element results by taking derivatives of the initially-linear regimes of the force-versus-deformation curves. Strictly speaking, a stiffness derived in this manner has contributions from both the bending stiffness and shear stiffness of the structure. However, in the structures examined, the bending stiffness contributions were assumed to be dominant; thus, the values could be directly compared to theoretically-predicted bending stiffnesses. As demonstrated by the exceptionally close match between finite element results and theoretical predictions, this assumption was sound.

The preceding assumption can also be theoretically justified as follows. From the theory

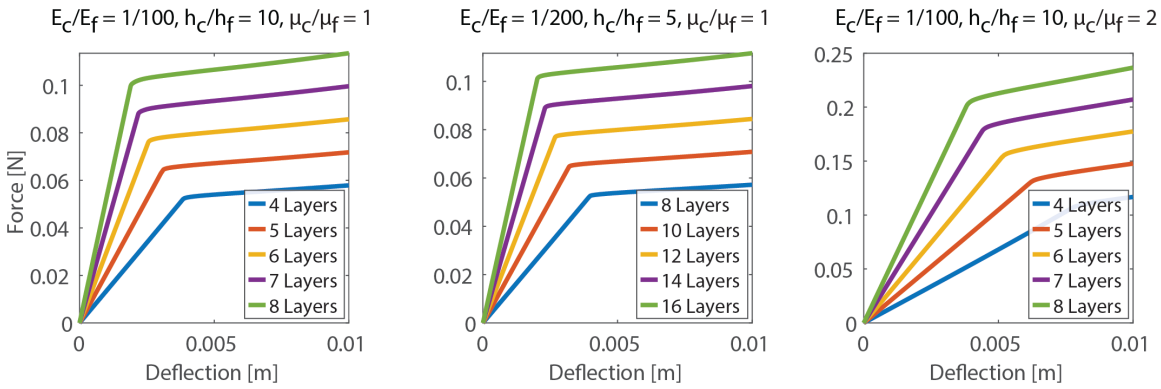

Figure S4: Force-versus-deflection curves extracted from finite element simulations. These plots were used to calculate performance metrics, which were compared to theoretical predictions in **Figure 4**.

of partial deflections for sandwich beams,

$$w(x) = w_b(x) + w_s(x) \tag{67}$$

where $w(x)$ is the deflection of the sandwich beam as a function of the x-coordinate, $w_b(x)$ is the contribution from bending compliance, and $w_s(x)$ is the contribution from shear compliance[4].

If the sandwich beam is subject to a concentrated transverse force P, the deflection at a point $x = a$ can be written as

$$w(a) = \frac{PL^3}{\alpha D} + \frac{PL}{\beta S} \tag{68}$$

where L is the length of the beam, D is the bending stiffness (i.e., the constant of proportionality between the bending moment and the curvature), and S is the shear stiffness (i.e., the constant of proportionality between the average shear stress and the average shear strain), and α and β are constants that depend on the boundary conditions. For example, for the deflection at the midpoint of a beam in 3-point bending, $\alpha = 48$ and $\beta = 4$, and for the deflection at the end of a beam in cantilever tip loading, $\alpha = 3$ and $\beta = 1$.

For bending deflections to be dominant (i.e., shear deflections to be negligible),

$$\frac{\frac{L^3}{\alpha D}}{\frac{L}{\beta S}} >> 1 \tag{69}$$

For sandwich beams, $D = \frac{E_f \frac{f}{2}(c+\frac{f}{2})^2}{2}$ and $S = \frac{G_c(c+\frac{f}{2})^2}{c}$, where G_c is the shear modulus of the core. For linearly elastic materials, $G = \frac{E}{2(1+\nu)}$. Substituting these expressions into (69) and simplifying,

$$\frac{\beta}{\alpha}\frac{E_c}{E_f}\frac{2}{1+\nu_c}\frac{L^2}{cf} >> 1 \tag{70}$$

Among the structures examined in our finite element simulations, the left-hand side of the above equation has a minimum value of 75. Thus, bending stiffness is dominant.

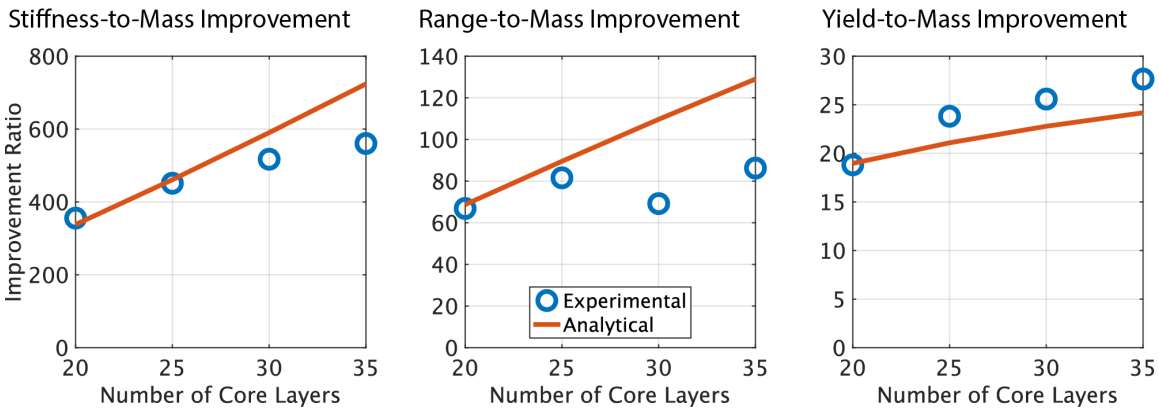

Figure S5: Comparison of experimentally-measured improvement ratios to theoretical predictions for a steel-paper sandwich jamming structure with multiple layer configurations.

3.2 Experimental Comparison

According to the procedure described earlier, steel-paper sandwich structures with 4 different layer configurations (i.e., 20, 25, 30, and 35 core layers) were tested in 3-point bending with vacuum on and off. Stiffness-to-mass, range-to-mass, and yield-to-mass improvement ratios were calculated from the data and compared to theoretical predictions. **Figure S5** shows the results. For each performance metric, the percentage error was also calculated as (Theoretical value − Experimental value) / (Theoretical value) ∗ 100%.

For all 3 performance metrics, the theoretical model predicted experimental results accurately for 20 and 25 layers, exhibiting a maximum error of 13%. However, the error was moderately large for the stiffness-to-mass improvement ratio at 35 layers (23%), as well as the range-to-mass improvement ratio at 30 and 35 layers (37% and 33%, respectively).

Through extensive experimental testing of the samples, it was determined that a primary cause of the stiffness and range discrepancies was inconsistent contact between adjacent layers due to 1) surface contaminants (e.g., grease particles), 2) curvature induced by the manufacturing process (e.g., shearing metal), and 3) localized (rather than global) buckling. These sources of error caused certain sections of the sandwich structure to be jammed and others to be unjammed, decreasing the effective bending stiffness and stiffness range of the structure. In addition, another cause of the range discrepancy was gravitational loading of the layers. The weight of the layers caused frictional coupling even when no vacuum was applied, thus reducing the measured stiffness range.

Future design efforts for sandwich jamming structures should focus on developing careful manufacturing processes to mitigate the sources of error leading to inconsistent contact. Until then, for performance-sensitive applications, the authors recommend introducing a factor of safety of 1.2 to 1.4 into the theoretically-predicted stiffness-to-mass and range-to-mass ratios for sandwich structures with high numbers of core layers (i.e., 30+).

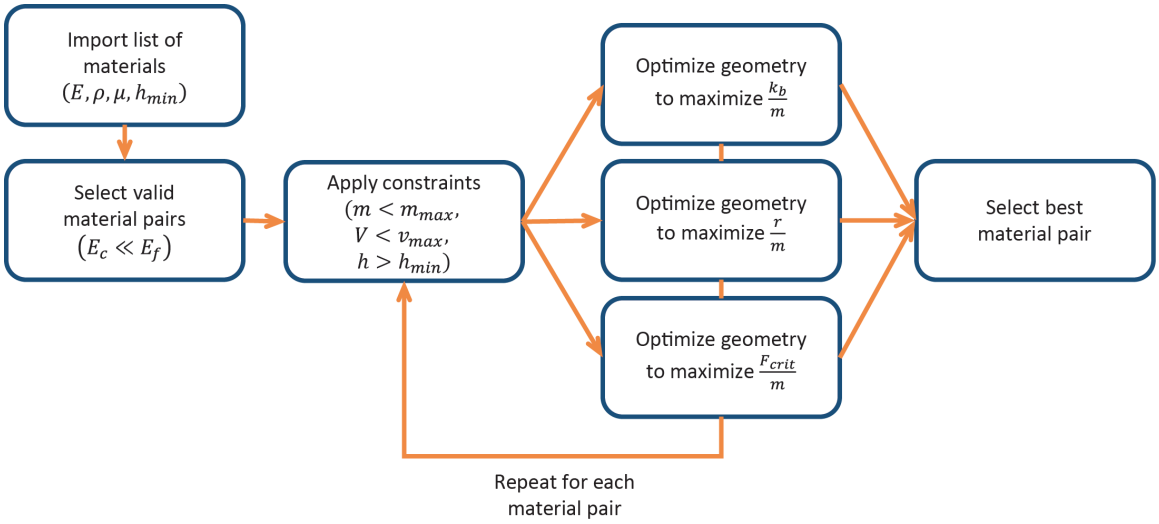

Figure S6: Flow chart of the critical steps in the software routine for optimizing sandwich jamming structures.

4 Optimization

4.1 Software Routine

A software routine to optimize sandwich jamming structures was constructed in mathematical analysis software (MATLAB 2018a); a flow chart of the routine is shown in **Figure S6**. First, the routine imports a list of materials and material properties that are provided by the user. For each material, the user must specify the elastic modulus E, the density ρ, the coefficient of friction μ, and the minimum material thickness h_{min}, as materials are not practically available in arbitrarily small thicknesses.

Next, the software routine cycles through each possible material pair and determines which pairs satisfy the assumptions of sandwich theory and recommended construction guidelines (i.e., $E_c << E_f$). For every satisfactory pair, the routine optimizes each performance metric (i.e., stiffness-to-mass, range-to-mass, and yield-to-mass) separately. The optimization algorithm is a constrained nonlinear algorithm based on gradient descent ($fmincon$). The constraints are mass and volume constraints specified by the user, as well as the h_{min} constraint described above. The optimized parameters are geometric variables (i.e., n_c, n_f, h_c, h_f, c, and f), and the cost functions are simply the reciprocals of the stiffness-to-mass, range-to-mass, and yield-to-mass expressions for sandwich jamming structures that were derived in **SI: Theoretical Modeling**.

4.2 Additional Data

Table S3 lists the materials and material properties that were used in the optimization case study. The material properties were derived from experimental measurements, as well as reference values available in online databases. The minimum thicknesses were defined by what was available for a low cost from an online mechanical parts vendor (i.e., McMaster-Carr[5]). **Table S4** and **Table S5** provide the optimization results for the stiffness-to-mass

Table S3: Materials and material properties used in the optimization case study.

	Input Parameter			
Material	$\rho[\frac{kg}{m^3}]$	$E[MPa]$	μ	$h_{min}[mm]$
Steel	8100	1.73e5	0.38	0.05
Paper	800	4.6e3	0.65	0.1
LDPE	840	2.8e2	0.18	0.1
PU Foam	480	4	0.38	0.79

Table S4: Results from the optimization case study for the stiffness-to-mass ratio. The first- and second-best performing material configurations were steel-foam and steel-paper, respectively.

	Optimized Parameter		
Material Configuration	n_c	n_f	Stiffness-to-Mass $[\frac{N*m^2}{kg}]$
Steel-Paper	66	2	1.7e3
Steel-LDPE	63	2	1.0e3
Steel-Foam	8	2	1.7e3
Paper-Foam	8	6	1.1e2
LDPE-Foam	8	6	6.3

and yield-to-mass ratios, respectively.

5 Demonstrations

5.1 Optimization and Fabrication

Prior to fabrication of the orthosis, the optimization software routine was used to determine the configuration of the sandwich jamming structure that would be integrated into the device. The materials considered were the same as those in the optimization case study; however, the minimum layer thickness for steel was adjusted to 0.025 mm (0.001") upon purchase of thin shim stock (9011K211, McMaster-Carr). A maximum mass constraint of 40 g was applied. In addition, in order to achieve comfort and security, the width and length of the laminar jamming structure were selected to be 25 mm and 150 mm, respectively; a maximum height constraint of 3.5 mm was then applied.

Optimized steel-paper sandwich jamming structures were found to provide an excellent balance of stiffness-to-mass, range-to-mass, and yield-to-mass behavior compared to other material configurations. The optimized structures consisted of 6 layers of 0.025 mm (0.001")-thick low-carbon steel, 30 layers of 0.1 mm (0.004")-thick paper, and 6 layers of steel. The wrist orthosis itself consisted of an elastic hand sleeve made of a copper-nylon

Table S5: Results from the optimization case study for the yield-to-mass ratio. The first- and second-best performing material configurations were paper-foam and LDPE-foam, respectively.

	Optimized Parameter		
Material Configuration	n_c	n_f	Yield-to-Mass $[\frac{N}{kg}]$
Steel-Paper	66	2	6.6e2
Steel-LDPE	63	2	1.7e2
Steel-Foam	8	2	5.1e2
Paper-Foam	9	2	1.1e3
LDPE-Foam	9	2	1.1e3

composite material (Copper Infused Wrist Sleeve, UptoFit Sports, Wilmington, DE) that was sewn to an arm sleeve constructed from a fabric-foam composite material with a non-slip interior coating (NuStim, Fabrifoam, Exton, PA).

5.2 Human Subject Testing

All experimental procedures were approved by the Harvard University Committee on the Use of Human Subjects. Nine healthy adult participants were recruited for the study.

5.2.1 Measurement of Maximum Voluntary Contraction

Subjects were asked to complete a maximum voluntary contraction (MVC) test with no orthosis. Three trials were conducted for each subject. In each trial, the subject was requested to bend their arm to 90 degrees and freely rest it on a flat surface. The subject was then asked to push their palm upward against a flat stationary surface as hard as possible. Muscle activation data was measured for 5 s using a portable surface electromyography system (TeleMyo 2400T G2, Noraxon U.S.A., Scottsdale, AZ) recording at 1500 Hz. The MVC was computed as the average EMG signal over all 3 trials. This value was then used to normalize the subject's average EMG signals during the isometric hold task, described below.

5.2.2 Isometric Hold Task

After resting, subjects were asked to complete the isometric hold tasks with no orthosis and with 2 orthosis configurations: a sandwich-jamming orthosis in the inactive (i.e., unjammed) state and a sandwich-jamming orthosis in the active (i.e., jammed) state. Three trials were conducted for each of the 3 configurations. In each trial, a 1 kg weight was suspended from the hand, and muscle activation data was recorded.

After the tests were conducted, the raw data was filtered using mathematical analysis software (MATLAB 2018a). First, a band-stop filter was applied between 58 Hz and 62 Hz to mitigate power-line noise. Next, a bandpass filter was applied with cutoff frequencies of

10 Hz and 350 Hz. The data was then rectified, and an envelope was fit to the resulting curves. **Figure 6E** shows EMG data for the isometric hold task for 1 human subject.

5.2.3 Range-of-Motion Test

Subjects were asked to complete range-of-motion tests with no orthosis and a sandwich jamming orthosis in the inactive state. During the tests, subjects were asked to flex and extend their wrists 3 times to the maximum angle that they still perceived as comfortable while remaining relaxed. A goniometer was used to manually measure the maximum flexion and extension angles during each cycle.

References

[1] Laminar Jamming Structures. `https://softroboticstoolkit.com/laminar-jamming`, 2018. Accessed: 2018-8-1.

[2] shadedErrorBar. `https://www.mathworks.com/matlabcentral/fileexchange/26311-raacampbell-shadederrorbar`, 2018. Accessed: 2017-8-1.

[3] YS Narang, JJ Vlassak, and RD Howe. Mechanically versatile soft machines through laminar jamming. *Advanced Functional Materials*, 28(17), 2018.

[4] D Zenkert. *Handbook of Sandwich Construction*. Engineering Materials Advisory Services Ltd., 1997.

[5] McMaster-Carr. `https://www.mcmaster.com/`, 2018. Accessed: 2018-8-1.